Journal of Computational Physics 315 (2016) 409–433

Contents lists available at ScienceDirect

Journal of Computational Physics

www.elsevier.com/locate/jcp

Junction-Generalized Riemann Problem for stiff hyperbolic balance laws in networks: An implicit solver and ADER schemes

Christian Contarino [a,*], Eleuterio F. Toro [b], Gino I. Montecinos [c], Raul Borsche [d], Jochen Kall [d]

[a] Department of Mathematics, University of Trento, via Sommarive 14, 38123 Povo (Trento), Italy
[b] Laboratory of Applied Mathematics, University of Trento, via Mesiano 77, 38123 Mesiano (Trento), Italy
[c] Center for Mathematical Modeling (CMM), Universidad de Chile, Beauchef 851, Edificio Norte, Piso 7, Santiago, Chile
[d] Fachbereich Mathematik, Technische Universität Kaiserslautern, Erwin Schrödinger Straße, Building 48, 67663 Kaiserslautern, Germany

ARTICLE INFO

Article history:
Received 18 December 2015
Received in revised form 10 March 2016
Accepted 21 March 2016
Available online 24 March 2016

Keywords:
Junction-generalized Riemann problem
ADER schemes
High-order coupling
Stiff source term
Junctions
Network of hyperbolic balance laws

ABSTRACT

In this paper we design a new implicit solver for the Junction-Generalized Riemann Problem (J-GRP), which is based on a recently proposed implicit method for solving the Generalized Riemann Problem (GRP) for systems of hyperbolic balance laws. We use the new J-GRP solver to construct an ADER scheme that is globally explicit, locally implicit and with no theoretical accuracy barrier, in both space and time. The resulting ADER scheme is able to deal with stiff source terms and can be applied to non-linear systems of hyperbolic balance laws in domains consisting on networks of one-dimensional sub-domains. In this paper we specifically apply the numerical techniques to networks of blood vessels. We report on a test problem with exact solution for a simplified network of three vessels meeting at a single junction, which is then used to carry out a systematic convergence rate study of the proposed high-order numerical methods. Schemes up to fifth order of accuracy in space and time are implemented and tested. We then show the ability of the ADER scheme to deal with stiff sources through a numerical simulation in a network of vessels. An application to a physical test problem consisting of a network of 37 compliant silicon tubes (arteries) and 21 junctions, reveals that it is imperative to use high-order methods at junctions, in order to preserve the desired high order of accuracy in the full computational domain. For example, it is demonstrated that a second-order method throughout, gives comparable results to a method that is fourth order in the interior of the domain and first order at junctions.

1. Introduction

In recent years, suitable computational methods for non-linear systems of hyperbolic balance laws in domains consisting on networks of one-dimensional sub-domains, have been the subject of many publications. Related applications include gas flow in pipes [1–3], traffic flow [4–6], water flow [7,8] and blood flow in the human circulation system [9–17]. For a review

* Corresponding author.
E-mail address: christian.contarino@unitn.it (C. Contarino).

http://dx.doi.org/10.1016/j.jcp.2016.03.049
0021-9991/

of the subject see [18]. In all of these, the crucial point is the coupling of the information of the various one-dimensional sub-domains converging into a single junction. There exists a class of multi-scale methods that are based on the coupling between two or three-dimensional and one-dimensional equations. For the Euler equations, Hong and Kim [19] described a strategy to simulate a network of pipes where the junction interfaces are modeled through the three-dimensional equations and normal averaged fluxes are used as boundary condition for the one-dimensional equations. Formaggia et al. [20] proposed an approach to couple the three-dimensional and one-dimensional Navier–Stokes equations for flow problems in compliant vessels. Miglio et al. [21,22] coupled the two-dimensional and the one-dimensional Saint-Venant equations for water flow. With a multi-scale approach, one can maintain the information of the geometry such as angles and secondary flows, but as the number of junctions increases and the geometry becomes more complex, the computational cost can become too large, making a real simulation difficult or unfeasible. An example of a simpler model was described by Fullana et al. [23] for blood flow that consists of ingoing and outgoing flows in a tank with a time-variable volume V, with a tube law analogous to the vessel tube law that relates pressure and volume. In this case, the choice of the tube law and parameters causes the numerical simulation to be parameter-dependent.

The coupling of different one-dimensional sub-domains at a junction has been formulated as an extended Riemann problem, see [24–26]. This formulation has several advantages. Firstly, it allows for a rigorous study of existence and uniqueness of solutions. Secondly, it can be used to numerically connect different tubes or channels, and can be combined with a numerical scheme for the interior part without additional computational costs compared to a multi-scale approach. Thirdly, it does not depend on additional parameters and the coupling conditions with no energy losses arise naturally from the PDEs themselves. The main disadvantage of this approach is the lack of geometrical information such as angles. For a rigorous mathematical study of existence and uniqueness of the Riemann problem solution at a junction under the assumption of subcritical flows, see Colombo et al. [24–26]. For the solution of the Riemann problem at a junction for arteries see [27], for arteries and veins refer to [9] and for gas pipes see [1,28].

A lot of research has been carried out in recent years in high-order ADER methods for both linear and non-linear systems in one, two and three space dimensions using either Cartesian or unstructured meshes, see for instance [29–36]. The building block of the ADER methodology is the solution of the Generalized Riemann Problem (GRP). Several solvers for the GRP have been proposed in the literature. The first one was proposed by Toro and Titarev [37], called here the Toro–Titarev (TT) solver. Then, Castro and Toro [38] reinterpreted, in the context of the GRP, the numerical scheme suggested by Harten et al. [39] and proposed the HEOC solver. In the same study, the authors also proposed a different way to solve the GRP, which is analogous to the TT solver, and called it the Castro–Toro (CT) solver. Since all of these mentioned solvers are based on the explicit Taylor expansion combined with the Cauchy–Kowalewskaya procedure, they do not deal with stiff source terms. The first GRP solver that has allowed the proper treatment of stiff source terms was put forward by Dumbser, Enaux and Toro [40], called here the DET solver. Subsequently, Montecinos and Toro [41] proposed an implicit solver, which is based on the implicit Taylor expansion combined with the Cauchy–Kowalewskaya procedure and is able to handle stiff source terms. The authors called it the MT-TT solver. More recently, they have formulated in [42] the implicit version of the HEOC solver and called it the MT-HEOC solver.

The extension of the Classical Riemann Problem (CRP) for junctions, which we call throughout this paper the Junction-Classical Riemann Problem (J-CRP), has been studied and used in the context of low and high-order numerical schemes. A low order numerical treatment of junctions spoils the accuracy in space and time achieved by a high-order numerical scheme used within each sub-domain of the network. Examples of this, in the context of human blood circulation simulated through a mathematical model, can be seen for instance in Müller and Toro [9,10], Liang et al. [13–15] and Mynard et al. [16]. First-order errors travel through the network of vessels with a damping effect for the pressure pulse-waves. Moreover, Borsche and Kall [43] observed that the combination of schemes and coupling conditions of different orders may modify the speed at which shocks pass the junction. To date, few studies have been done on the solution of the Junction-Generalized Riemann Problem (J-GRP), namely the extension of the GRP for junctions connecting one-dimensional sub-domains. The first high-order solvers of the J-GRP were put forward by Borsche and Kall [43]. They generalized the TT and the CT solvers for the J-GRP. Then, Müller and Blanco [44] proposed an extension of the DET solver, which is able to deal with stiff source terms. In addition, Borsche and Kall [45] extended the HEOC solver for junctions. No studies have been done so far to extend the MT-TT or the MT-HEOC solvers.

The aim of this paper is to extend the MT-HEOC solver for the GRP and construct a new implicit, semi-analytical solution of the J-GRP. Using the new MT-HEOC solver for the J-GRP, we design an ADER scheme that is globally explicit, locally implicit, free of any theoretical accuracy barrier in space and time, able to deal with stiff source terms and can be applied to non-linear systems of hyperbolic balance laws in domains consisting on networks of one-dimensional sub-domains. To validate the numerical methodology, we carry out a convergence rate study for a network of three vessels, propose a numerical experiment that assesses the ability of the numerical scheme to deal with stiff source terms and junctions, and implement the method for the physical model presented by Matthys et al. [46] and further studied by Alastruey et al. [11].

The rest of this paper is structured as follows: in Section 2 we review the one-dimensional blood flow equations and explain the ADER finite volume scheme with different solvers for the GRP. We then describe a new methodology for solving the J-GRP. In Section 3 we propose two test problems in a network to verify the order of accuracy and the ability of the solver to deal with stiff source terms. We then show an application for a more complex network of 37 vessels and 21 junctions for which experimental results are available in the literature. Section 4 gives a summary and conclusions.

2. Methods

In this section we review the one-dimensional blood flow equations, briefly describe the ADER scheme with two different solvers for the GRP, formulate the J-GRP and propose a new methodology to accurately solve it.

2.1. One-dimensional blood flow equations

The one-dimensional blood flow equations for a compliant vessel are the following

$$\begin{cases} \partial_t A + \partial_x q = 0 \,, \\ \partial_t q + \partial_x \left(\alpha \frac{q^2}{A}\right) + \frac{A}{\rho}\partial_x p = -\frac{f}{\rho} \,, \end{cases} \tag{1}$$

where x is the space variable, t is time, α is the Coriolis coefficient assumed to be $\alpha = 1$, $A(x,t)$ is the cross-sectional area of the vessel, $q(x,t) = A(x,t)u(x,t)$ is the flow, $u(x,t)$ is the velocity, $p(x,t)$ is the pressure, ρ is the blood density (set to 1050 kg/m^3), $f(x,t) = \gamma \pi \mu \frac{q}{A}$ is the friction force per unit length of the tube with parameter γ chosen depending on the velocity profile and μ is the kinematic viscosity. There are two governing partial differential equations and three unknowns, namely $A(x,t)$, $q(x,t)$ and $p(x,t)$. For this reason, an extra relation is required to close the system, the *tube law*, which relates pressure $p(x,t)$ and cross-sectional area $A(x,t)$. A purely elastic tube law reads

$$p(x,t) = K(x)\psi(A(x,t); A_0(x)) + p_e(x,t) \,, \tag{2}$$

with

$$\psi(A(x,t); A_0(x)) = \left[\left(\frac{A(x,t)}{A_0(x)} \right)^m - \left(\frac{A(x,t)}{A_0(x)} \right)^n \right], \tag{3}$$

where $p_e(x,t)$ is the external pressure, $A_0(x)$ is vessel cross-sectional area at equilibrium, $K(x)$ is the bending stiffness of the vessel wall, $m \geq 0$ and $n \leq 0$ are real numbers to be specified. For hyperbolicity m and n must satisfy additional constraints, see [47]. For more information about the mathematical structure of the equations, see [48,47]. Relation (2) models a purely elastic behavior of the vessel wall. Other tube laws may also account for visco-elasticity, elastin and collagen, see [11,49]. Practical choices for the parameters m, n and K are

$$K(x) = \begin{cases} K_a = \dfrac{E}{1-\nu^2}\left(\dfrac{h_0}{r_0}\right), & m = \dfrac{1}{2}\,, \quad n = 0 \quad \text{for arteries,} \\ K_v = \dfrac{E}{12(1-\nu^2)}\left(\dfrac{h_0}{r_0}\right)^3, & m \approx 10\,, \quad n = -3/2 \quad \text{for veins,} \end{cases} \tag{4}$$

where ν, h_0, r_0 are the Poisson ratio (set to $\nu = 0.5$), the wall-thickness at equilibrium and the cross-sectional radius at equilibrium. It is possible to write the blood flow equations in conservative form as follows:

$$\partial_t \mathbf{Q} + \partial_x \mathbf{F}(\mathbf{Q}, x) = \mathbf{S}(\mathbf{Q}, x) \,, \tag{5}$$

where

$$\mathbf{Q} = \begin{bmatrix} A \\ Au \end{bmatrix}, \quad \mathbf{F}(\mathbf{Q}, x) = \begin{bmatrix} Au \\ Au^2 - \frac{K}{\rho} A_0 \partial_{A_0} \Psi \end{bmatrix}, \tag{6}$$

$$\mathbf{S}(\mathbf{Q}, x) = \begin{bmatrix} 0 \\ -\frac{1}{\rho}\left(f + A\partial_x p_e + \Psi \partial_x K + K \partial_x A_0 \partial_{A_0} \Psi \right) \end{bmatrix}, \tag{7}$$

with

$$\Psi = \Psi(A; A_0) = \int_A \psi(A; A_0) \mathrm{d}A = A_0 \left(\frac{1}{m+1}\left(\frac{A}{A_0}\right)^{m+1} - \frac{1}{n+1}\left(\frac{A}{A_0}\right)^{n+1} \right), \tag{8}$$

and

$$\partial_{A_0}\Psi = \partial_{A_0}\Psi(A; A_0) = \partial_{A_0} \int_A \psi(A; A_0) \mathrm{d}A = -\left(\frac{m}{m+1}\left(\frac{A}{A_0}\right)^{m+1} - \frac{n}{n+1}\left(\frac{A}{A_0}\right)^{n+1} \right). \tag{9}$$

The constants arising from the integrals (8) and (9) are set to zero for consistency with (1) and (2), see [50–52]. For a complete view of the mathematical analysis and derivation of the one-dimensional blood flow equations, refer to [47,48,52].

2.2. ADER finite volume scheme

Consider the system of m hyperbolic balance laws

$$\partial_t \mathbf{Q} + \partial_x \mathbf{F}(\mathbf{Q}) = \mathbf{S}(\mathbf{Q}) \,. \tag{10}$$

By integrating (10) over the control volume $V = [x_{i-\frac{1}{2}}, x_{i+\frac{1}{2}}] \times [t^n, t^{n+1}]$ we obtain the exact formula

$$\mathbf{Q}_i^{n+1} = \mathbf{Q}_i^n - \frac{\Delta t}{\Delta x}\left(\mathbf{F}_{i+\frac{1}{2}} - \mathbf{F}_{i-\frac{1}{2}}\right) + \Delta t \mathbf{S}_i \,, \tag{11}$$

with definitions

$$\mathbf{Q}_i^n = \frac{1}{\Delta x}\int_{x_{i-\frac{1}{2}}}^{x_{i+\frac{1}{2}}} \mathbf{Q}(x, t^n)\mathrm{d}x \,, \tag{12}$$

$$\mathbf{F}_{i+\frac{1}{2}} = \frac{1}{\Delta t}\int_{t^n}^{t^{n+1}} \mathbf{F}(\mathbf{Q}(x_{i+\frac{1}{2}}, \tau))\mathrm{d}\tau \,, \quad \mathbf{S}_i = \frac{1}{\Delta t \Delta x}\int_{t^n}^{t^{n+1}}\int_{x_{i-\frac{1}{2}}}^{x_{i+\frac{1}{2}}} \mathbf{S}(\mathbf{Q}(x, \tau))\mathrm{d}x\mathrm{d}\tau \,. \tag{13}$$

Eq. (12) gives the spatial-integral average at time $t = t^n$ of the conserved variable $\mathbf{Q}$, (13) the time-integral average at interface $x = x_{i+\frac{1}{2}}$ of the physical flux $\mathbf{F}$ and the volume-integral average in V of the source term $\mathbf{S}$ respectively. Spatial mesh size and time step are $\Delta x = x_{i+\frac{1}{2}} - x_{i-\frac{1}{2}}$ and $\Delta t = t^{n+1} - t^n$ respectively. Finite volume methods depart from (10) to (13), where integrals are approximated, and then formula (11) becomes a *finite volume method*, where the approximated integrals (13) are called *numerical flux* and *numerical source*, respectively. The ADER finite volume schemes are one-step, fully discrete schemes, based on (11) with three main ingredients: a high-order spatial reconstruction (once per time step), the solution of the GRP at the cell interface to find the numerical flux and computation of the numerical source. The numerical flux is evaluated as time-integral average of the physical flux evaluated at the solution of the local GRP at the cell interface $x_{i+\frac{1}{2}}$ and the numerical source is computed as a high-order space–time integral of the source term within control volume V. See Toro et al. [29], Chapters 19 and 20 of [53] and references therein.

2.2.1. Generalized Riemann problem (GRP)

The Generalized Riemann Problem (GRP) is the following initial value problem

$$\left.\begin{aligned} &\text{PDEs:} \quad \partial_t \mathbf{Q} + \partial_x \mathbf{F}(\mathbf{Q}) = \mathbf{S}(\mathbf{Q}) \,, \quad x \in (-\infty, +\infty) \,, \quad t > 0, \\ &\text{ICs:} \quad \mathbf{Q}(x, 0) = \begin{cases} \mathbf{Q}_L(x) & x < 0 \,, \\ \mathbf{Q}_R(x) & x > 0 \,, \end{cases} \end{aligned}\right\} \tag{14}$$

where $\mathbf{Q}_L(x)$ and $\mathbf{Q}_R(x)$ are smooth vector-valued functions (e.g. polynomials of degree M) given by a reconstruction procedure. The particular case in which $\mathbf{Q}_L(x)$ and $\mathbf{Q}_R(x)$ are constant and $\mathbf{S}(\mathbf{Q}) = 0$ is called the *Classical Riemann Problem (CRP)*.

We are interested in finding the solution in time of problem (14) at the interface $x = 0$, which we denote with $\mathbf{Q}_{LR}(\tau)$, to evaluate the numerical flux $\mathbf{F}_{i+\frac{1}{2}}$, namely

$$\mathbf{F}_{i+\frac{1}{2}} = \frac{1}{\Delta t}\int_{t^n}^{t^{n+1}} \mathbf{F}(\mathbf{Q}_{LR}(\tau))\mathrm{d}\tau \,. \tag{15}$$

Several approaches have been proposed in the literature. There are two categories of GRP solvers: explicit and implicit. The first explicit solver for the GRP is the TT solver, proposed by Toro and Titarev [37]. Then, Castro and Toro proposed both the CT and the HEOC solvers [38]. The first implicit solver is the DET solver, proposed by Dumbser et al. [40]. Then, implicit versions of TT and HEOC resulted in the MT-TT and the MT-HEOC solvers, both proposed by Montecinos and Toro [41,42]. For a comparison between different GRP solvers see [54]. For a study of analytical properties of the TT solver see Goetz and Iske [55]. Here we briefly present the HEOC approach in the explicit and implicit forms.

2.2.2. The Harten–Engquist–Osher–Chakravarthy (HEOC) solver

Castro and Toro [38] reinterpreted the methodology proposed by Harten et al. [39] in terms of a local GRP. The idea is to first evolve in time, independently, the left and right extrapolated values at the interface of the left and right reconstructed polynomials, up to a time τ and then solve a CRP with the resulting piece-wise constant data. Then the sought GRP solution at time τ is the Godunov state of the CRP solution, that is, the solution along the t-axis of the CRP. In what follows we describe the full procedure.

The GRP solution along the t-axis $\mathbf{Q}_{LR}(\tau)$ of (14) is found by solving the following CRP

$$\left.\begin{aligned} &\text{PDEs:} \quad \partial_t \mathbf{Q} + \partial_x \mathbf{F}(\mathbf{Q}) = \mathbf{0}\,, \quad x \in (-\infty, +\infty)\,, \quad t > 0\,, \\ &\text{ICs:} \quad \mathbf{Q}(x,0) = \begin{cases} \hat{\mathbf{Q}}_L(\tau) & x < 0\,, \\ \hat{\mathbf{Q}}_R(\tau) & x > 0\,, \end{cases} \end{aligned}\right\} \tag{16}$$

where the evolved vectors $\hat{\mathbf{Q}}_L(\tau)$ and $\hat{\mathbf{Q}}_R(\tau)$ are constant and given by applying a Taylor expansion around the initial points $\mathbf{Q}_L(0_-) = \lim_{x\to 0_-} \mathbf{Q}_L(x)$ and $\mathbf{Q}_R(0_+) = \lim_{x\to 0_+} \mathbf{Q}_R(x)$, respectively, evaluated at τ, that is

$$\left.\begin{aligned} \hat{\mathbf{Q}}_L(\tau) &= \mathbf{Q}_L(0_-) + \sum_{j=1}^{M} \frac{\tau^j}{j!} \partial_t^{(j)} \mathbf{Q}_L(0_-)\,, \\ \hat{\mathbf{Q}}_R(\tau) &= \mathbf{Q}_R(0_+) + \sum_{j=1}^{M} \frac{\tau^j}{j!} \partial_t^{(j)} \mathbf{Q}_R(0_+)\,. \end{aligned}\right\} \tag{17}$$

The Cauchy–Kowalewskaya procedure allows us to use the PDEs in (14) to express all time derivatives in (17) as functionals of space derivatives and of the source term $\mathbf{S}(\mathbf{Q})$, namely

$$\partial_t^{(j)} \mathbf{Q}(x,t) = \mathbf{G}^{(j)}\Big(\mathbf{Q}(x,t), \ldots, \partial_x^{(j)} \mathbf{Q}(x,t)\Big)\,. \tag{18}$$

The polynomials $\mathbf{Q}_L(x)$ and $\mathbf{Q}_R(x)$ are defined on the left and right sides of the interface and are smooth away from 0 (locally the interface). This allows us to define limiting values from the left and right, at $t = 0$, of the spatial derivatives of the initial conditions, namely

$$\left.\begin{aligned} \partial_x^{(j)} \mathbf{Q}_L(0_-) &:= \lim_{x\to 0_-} \partial_x^{(j)} \mathbf{Q}_L(x)\,, \quad j = 1, \ldots, M\,, \\ \partial_x^{(j)} \mathbf{Q}_R(0_+) &:= \lim_{x\to 0_+} \partial_x^{(j)} \mathbf{Q}_R(x)\,, \quad j = 1, \ldots, M\,. \end{aligned}\right\} \tag{19}$$

Thus, time derivatives can be replaced by their respective Cauchy–Kowalewskaya functional $\mathbf{G}^{(j)}$, leading to

$$\left.\begin{aligned} \hat{\mathbf{Q}}_L(\tau) &= \mathbf{Q}_L(0_-) + \sum_{j=1}^{M} \frac{\tau^j}{j!} \mathbf{G}^{(j)}\Big(\mathbf{Q}_L(0_-), \ldots, \partial_x^{(j)} \mathbf{Q}_L(0_-)\Big)\,, \\ \hat{\mathbf{Q}}_R(\tau) &= \mathbf{Q}_R(0_+) + \sum_{j=1}^{M} \frac{\tau^j}{j!} \mathbf{G}^{(j)}\Big(\mathbf{Q}_R(0_+), \ldots, \partial_x^{(j)} \mathbf{Q}_R(0_+)\Big)\,. \end{aligned}\right\} \tag{20}$$

Eqs. (20) are final product of the *evolution stage*. The sought GRP solution along the t-axis at time $t = \tau$ is the Godunov state of the CRP with initial data given by (20) and self-similar solution $\mathbf{D}(x/t)$, that is

$$\mathbf{Q}_{LR}(\tau) = \mathbf{D}(0)\,. \tag{21}$$

Note that when solving the CRP (16) at time $t = \tau$, we change to local coordinates $\hat{x} = x$ and $\hat{t} = t - \tau$, and then for convenience we omit the "hats". This numerical solver for the GRP is called the *Harten–Engquist–Osher–Chakravarthy (HEOC)*. To evaluate the numerical flux $\mathbf{F}_{i+\frac{1}{2}}$, one has to calculate the solution of the GRP at the interface $x_{i+\frac{1}{2}}$ at different time-integration points, within the time step $0 \le \tau \le \Delta t$. In the HEOC solver, for each time-integration point, one has to apply two Taylor expansions and solve a CRP. Moreover, the HEOC solver requires a robust and generally non-linear Riemann solver, which can be time-consuming; whereas the TT solver needs a single expansion right at the interface and uses a non-linear Riemann solver only once to compute the leading term. To solve the CRP we recommend the use of a non-linear complete approximate Riemann solver. Here for the two equation model, we use the Harten–Lax–van Leer (HLL) [56]. For background on classical Riemann solvers, see [53].

We now describe the implicit version of the HEOC solver, which uses the implicit Taylor series expansion instead of the explicit version.

2.2.3. The MT implicit Taylor series expansion

Toro and Montecinos proposed in [42,41] two methodologies for solving the GRP: the MT-TT and the MT-HEOC solvers. These solvers are the implicit versions of the TT and the HEOC solvers respectively, and are able to deal with stiff source terms. They are based on an implicit Taylor expansion in the evolution stage, which generates non-linear algebraic problems to be solved. For the MT-HEOC approach there are two possible schemes, namely *Reduced Implicit Taylor expansion Approach (RITA)* and *Complete Implicit Taylor expansion Approach (CITA)*. See [42] for details. Here we describe the RITA approach, insofar as it is simpler and there are less operations to be performed, when compared to CITA.

First of all, we apply an implicit Taylor expansion at position $x = 0$ and time $t = \tau$,

$$\mathbf{Q}(0,\tau) = \mathbf{Q}(0,0_+) - \sum_{j=1}^{M} \frac{(-\tau)^j}{j!} \partial_t^{(j)} \mathbf{Q}(0,\tau)\,, \tag{22}$$

where the evolved vectors $\mathbf{Q}(0,\tau),\ldots,\partial_t^{(M)}\mathbf{Q}(0,\tau)$ are unknown. Then we use the Cauchy–Kowalewskaya procedure to convert time derivatives into functionals of space derivatives

$$\mathbf{Q}(0,\tau) = \mathbf{Q}(0,0_+) - \sum_{j=1}^{M} \frac{(-\tau)^j}{j!} \mathbf{G}^{(j)}\Big(\mathbf{Q}(0,\tau),\ldots,\partial_x^{(j)}\mathbf{Q}(0,\tau)\Big)\,. \tag{23}$$

Note that the Cauchy–Kowalewskaya functionals $\mathbf{G}^{(j)}$ are evaluated at the unknown evolved vectors $\mathbf{Q}(0,\tau),\ldots,\partial_x^{(j)}\mathbf{Q}(0,\tau)$. In Eqs. (23) there are $M+1$ vector unknowns and each one has m entries, thus the total number of unknowns is $m(M+1)$. Since we only have m equations in (23), we still need mM equations, which can be obtained by applying a time implicit Taylor expansion for the spatial derivatives $\partial_x^{(h)}\mathbf{Q}(0,\tau)$, with $h = 1,\ldots,M$, leading to

$$\partial_x^{(h)}\mathbf{Q}(0,\tau) = \partial_x^{(h)}\mathbf{Q}(0,0_+) - \sum_{j=1}^{M-h} \frac{(-\tau)^j}{j!} \partial_t^{(j)} \partial_x^{(h)} \mathbf{Q}(0,\tau)\,, \quad h = 1,\ldots,M\,. \tag{24}$$

Exchanging temporal and spatial derivatives and using the Cauchy–Kowalewskaya procedure, we obtain

$$\partial_x^{(h)}\mathbf{Q}(0,\tau) = \partial_x^{(h)}\mathbf{Q}(0,0_+) - \sum_{j=1}^{M-h} \frac{(-\tau)^j}{j!} \partial_x^{(h)} \mathbf{G}^{(j)}\Big(\mathbf{Q}(0,\tau),\ldots,\partial_x^{(j)}\mathbf{Q}(0,\tau)\Big)\,, \quad h = 1,\ldots,M\,. \tag{25}$$

The Mm and m equations obtained respectively by Eqs. (25) and (23) allow us to have the required number of equations, that is, $m(M+1)$. We introduce the notation

$$\left.\begin{array}{l} \mathbf{U} = [\mathbf{U}^0,\ldots,\mathbf{U}^M]\,, \quad \mathbf{U}^j = \partial_x^{(j)}\mathbf{Q}(0,\tau)\,, \quad j = 0,\ldots,M\,, \\ \mathbf{U}_0 = [\mathbf{U}_0^0,\ldots,\mathbf{U}_0^M]\,, \quad \mathbf{U}_0^j = \partial_x^{(j)}\mathbf{Q}(0,0_+)\,, \quad j = 0,\ldots,M\,, \end{array}\right\} \tag{26}$$

where $\mathbf{U}$ is the vector of unknown and $\mathbf{U}_0$ is a known vector of the leading terms. Hence, rewriting Eqs. (23) and (25), we end up with the following problem: given $\mathbf{U}_0$, find $\hat{\mathbf{U}}$ such that

$$\mathbf{L}(\hat{\mathbf{U}};\mathbf{U}_0,\tau) = \hat{\mathbf{U}} - \mathbf{H}(\hat{\mathbf{U}};\mathbf{U}_0,\tau) = \mathbf{0}\,, \tag{27}$$

where

$$\mathbf{H}(\mathbf{U};\mathbf{U}_0,\tau) = \begin{bmatrix} \mathbf{U}_0^0 - \displaystyle\sum_{j=1}^{M} \frac{(-\tau)^j}{j!} \mathbf{G}^{(j)}(\mathbf{U}^0,\ldots,\mathbf{U}^j) \\ \vdots \\ \mathbf{U}_0^h - \displaystyle\sum_{j=1}^{M-h} \frac{(-\tau)^j}{j!} \partial_x^{(h)} \mathbf{G}^{(j)}(\mathbf{U}^0,\ldots,\mathbf{U}^j) \\ \vdots \\ \mathbf{U}_0^M \end{bmatrix} \tag{28}$$

Once problem (27) is solved, evolved values $\mathbf{Q}(0,\tau),\ldots,\partial_x^{(M)}\mathbf{Q}(0,\tau)$ are known. Functionals $\mathbf{G}^{(j)}$ and their spatial derivatives can be found using symbolic manipulators in a preprocessing step. To find the root of $\mathbf{L}$, one can apply, for instance, a Newton or a Newton reduced-step method, see [42]. A possible guess value for a numerical method to find the solution of (27) is the vector of the leading terms, namely $\mathbf{U}_0$. The operator $\mathbf{L}(\hat{\mathbf{U}};\mathbf{U}_0,\tau)$ depends on the time τ and on the choice of $\mathbf{U}_0$, which will be different depending on the solver being used.

2.2.4. The implicit Montecinos–Toro HEOC (MT-HEOC) solver

The GRP solution along the t-axis $\mathbf{Q}_{LR}(\tau)$ of (14) is found by solving the following CRP

$$\left.\begin{array}{ll} \text{PDEs:} & \partial_t \mathbf{Q} + \partial_x \mathbf{F}(\mathbf{Q}) = \mathbf{0}\,, \quad x \in (-\infty, +\infty)\,, \quad t > 0\,, \\ \text{ICs:} & \mathbf{Q}(x,0) = \begin{cases} \hat{\mathbf{Q}}_L(\tau) & x < 0\,, \\ \hat{\mathbf{Q}}_R(\tau) & x > 0\,, \end{cases} \end{array}\right\} \tag{29}$$

where the evolved vectors $\hat{\mathbf{Q}}_L(\tau)$ and $\hat{\mathbf{Q}}_R(\tau)$ are constant and found by solving the following non-linear problems: find $\hat{\mathbf{U}}_L$ and $\hat{\mathbf{U}}_R$ such that

$$\mathbf{L}(\hat{\mathbf{U}}_L; \mathbf{U}_L, \tau) = \mathbf{0}\,, \quad \mathbf{L}(\hat{\mathbf{U}}_R; \mathbf{U}_R, \tau) = \mathbf{0}\,, \tag{30}$$

where the leading terms $\mathbf{U}_L$ and $\mathbf{U}_R$ are respectively

$$\left.\begin{array}{l} \mathbf{U}_L = [\mathbf{U}_L^0, \ldots, \mathbf{U}_L^M]\,, \quad \mathbf{U}_L^j = \partial_x^{(j)} \mathbf{Q}_L(0_-) = \lim\limits_{x \to 0_-} \partial_x^{(j)} \mathbf{Q}_L(x)\,, \quad j = 0, \ldots, M\,, \\ \mathbf{U}_R = [\mathbf{U}_R^0, \ldots, \mathbf{U}_R^M]\,, \quad \mathbf{U}_R^j = \partial_x^{(j)} \mathbf{Q}_R(0_+) = \lim\limits_{x \to 0_+} \partial_x^{(j)} \mathbf{Q}_R(x)\,, \quad j = 0, \ldots, M\,. \end{array}\right\} \tag{31}$$

The solution procedure of the non-linear problems (30) is termed here the *evolution stage*. Possible guess values for a numerical method to find the solutions of non-linear problems (30) are the reconstructed polynomials and their derivatives, namely $\mathbf{U}_L$ and $\mathbf{U}_R$. Once problems (30) are solved, then the evolved values $\hat{\mathbf{Q}}_L(\tau)$ and $\hat{\mathbf{Q}}_R(\tau)$ will be the first entries of $\hat{\mathbf{U}}_L$ and $\hat{\mathbf{U}}_R$ respectively, namely $\hat{\mathbf{U}}_L^0$ and $\hat{\mathbf{U}}_R^0$. The sought GRP solution along the t-axis at time $t = \tau$ is the Godunov state of the CRP (29) with initial data $\hat{\mathbf{Q}}_L(\tau)$ and $\hat{\mathbf{Q}}_R(\tau)$ and self-similar solution $\mathbf{D}(x/t)$, namely

$$\mathbf{Q}_{LR}(\tau) = \mathbf{D}(0)\,. \tag{32}$$

The MT-HEOC solver uses the implicit Taylor series expansion (30) in the evolution stage, instead of an explicit one (20). The use of the implicit approach in the evolution stage requires the solution of non-linear algebraic problem with $m(M+1)$ unknowns for each side of the interface and then the solution of a non-linear CRP. As for the HEOC solver, we can also use an approximate Riemann solver to find the solution of the CRP (29), such as the two-rarefaction [53] or the HLL Riemann solvers [56].

The PDEs of the CRP in (29) do not contain the source term $\mathbf{S}(\mathbf{Q})$. However, the influence of the source term is accounted for via the Cauchy–Kowalewskaya procedure through the functional $\mathbf{H}(\mathbf{U}; \mathbf{U}_0, \tau)$. The non-linear problems, which have to be solved in order to find the initial condition for the CRP, allow us to deal with stiff source terms, see [41,42] and [57].

2.3. The Junction-Generalized Riemann Problem (J-GRP)

We are concerned with the design of high-order numerical methods for solving hyperbolic balance laws in simplified domains consisting of networks of one-dimensional sub-domains that can be, for example, blood vessels, water channels or gas tubes. In our application we formulate the J-GRP in the context of one-dimensional blood flow equations. For this reason, we formulate the mathematical problem in terms of vessels. First, we define the J-GRP, then we explain how to solve the J-CRP for one-dimensional blood flow equations and propose a new solver for the J-GRP.

Consider a set of N vessels with the common vertex V. For the k-th vessel, variable x^k is the local coordinate and the vertex V is located in 0 without loss of generality. In each k-th vessel, consider the following initial value problem

$$\left.\begin{array}{ll} \text{PDEs:} & \partial_t \mathbf{Q}^k + \partial_x \mathbf{F}(\mathbf{Q}^k) = \mathbf{S}(\mathbf{Q}^k)\,, \quad x^k \in I_k = \left(a^k, b^k\right)\,, \quad t > 0\,, \\ \text{ICs:} & \mathbf{Q}^k(x^k, 0) = \mathbf{Q}^k_{(0)}(x^k)\,, \end{array}\right\} \tag{33}$$

where either a^k or b^k is the local coordinate of vertex V, spatial domain I_k has length $L^k = |b^k - a^k|$ and the initial condition $\mathbf{Q}^k_{(0)}(x^k)$ is a smooth vector-valued function of the local coordinate x^k (e.g. polynomials of order M). Note that the material and geometrical properties can be different for each k-th vessel. The set of solutions $\mathbf{Q}^k(x^k, t)$, with $k = 1, \ldots, N$, has to satisfy the following coupling conditions at the common vertex V

$$\mathbf{\Phi}(\mathbf{Q}^1(0,t), \ldots, \mathbf{Q}^N(0,t)) = \mathbf{0}\,, \quad t > 0\,, \tag{34}$$

where the vector $\mathbf{\Phi}$ defines coupling conditions. We define as *Junction-Generalized Riemann Problem (J-GRP)* at the vertex V with N vessels, the set initial value problems (33), with $k = 1 \ldots, N$, with constraints (34). Fig. 1 illustrates a simple representation of a J-GRP. For the particular case in which $N = 2$, $b^1 = 0$ and $a^2 = 0$, we end up with a GRP with the jump discontinuity at the initial time located in $x = 0$. Therefore, the J-GRP is an extension of the GRP. In order to easy the notation in the following, we shall consider the local coordinate x^k without index.

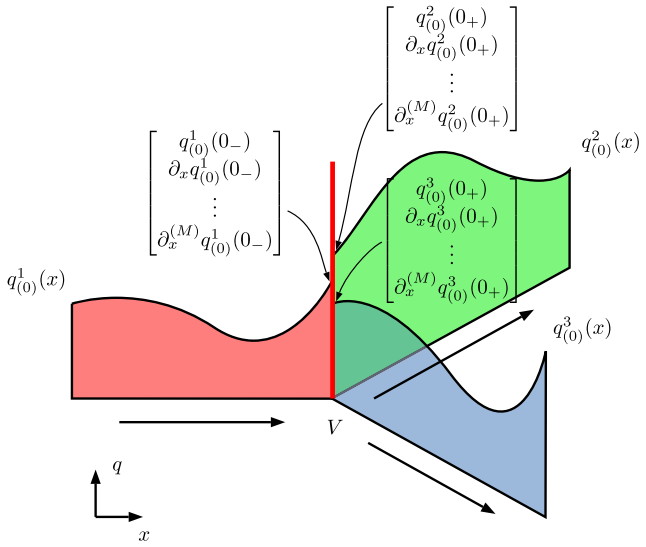

Fig. 1. Illustration of initial condition for a J-GRP with $N = 3$ vessels and vertex V for a single component $q_{(0)}(x,t)$ of the vector of unknowns $\mathbf{Q}_{(0)}(x,t)$. The data $q^1_{(0)}$, $q^2_{(0)}$ and $q^3_{(0)}$ are smooth away from vertex V and have one-sided spatial derivatives at V.

We are interested in finding the solutions in time of problem (33) at the vertex V, which we denote with $\mathbf{Q}^k_V(\tau)$, for $k = 1, \ldots, N$, to evaluate the numerical flux $\mathbf{F}^k_V$ of the k-th vessel at the vertex V, namely

$$\mathbf{F}^k_V = \frac{1}{\Delta t} \int_{t^n}^{t^{n+1}} \mathbf{F}(\mathbf{Q}^k_V(\tau)) \mathrm{d}\tau \ . \tag{35}$$

In the following we shall refer to these numerical fluxes at the vertex V as the *junction-numerical fluxes*. The main ingredient we require to solve the J-GRP is the related *classical* version with piece-wise constant data and no source terms.

2.3.1. The Junction-Classical Riemann Problem (J-CRP)

Consider the following set of initial value problems

$$\left.\begin{array}{ll} \text{PDEs:} & \partial_t \mathbf{Q}^k + \partial_x \mathbf{F}(\mathbf{Q}^k) = \mathbf{0} \,, \quad x \in I_k = \left(a^k, b^k\right) \,, \quad t > 0 \,, \\ \text{ICs:} & \mathbf{Q}^k(x,0) = \mathbf{Q}^k_{(0)} \,, \end{array}\right\} \quad k = 1, \ldots, N \,, \tag{36}$$

with coupling conditions $\mathbf{\Phi}$

$$\mathbf{\Phi}(\mathbf{Q}^1(0,t), \ldots, \mathbf{Q}^N(0,t)) = \mathbf{0} \,, \quad t > 0 \,, \tag{37}$$

where $\mathbf{Q}^k_{(0)}$, with $k = 1, \ldots, N$, are constant vectors. We define as *Junction-Classical Riemann Problem (J-CRP)* at the vertex V with N vessels, the set initial value problems (36), with $k = 1 \ldots, N$, with constraints (37).

The solution of a J-CRP is a set of self-similar functions $\mathbf{D}^k(x/t)$ defined for each k-th vessel. For a 2×2 hyperbolic balance law system in subcritical regime, we have a total number of $2N$ states. These $2N$ states arise from the N initial conditions $\mathbf{Q}^k_{(0)}$, with $k = 1, \ldots, N$, and N states $\mathbf{Q}^k_*$, with $k = 1, \ldots, N$, which are connected to the initial conditions through non-linear waves and among themselves by the coupling conditions $\mathbf{\Phi}$. To completely solve the J-CRP, one has to find values $\mathbf{Q}^k_*$, with $k = 1, \ldots, N$, using both the structure of the waves (i.e. rarefactions or shocks) and the coupling conditions $\mathbf{\Phi}$. The solutions along the t-axis $\mathbf{D}^k(0)$, with $k = 1, \ldots, N$, of the J-CRP, are termed here the *Godunov states*.

Here we present the solution of the J-CRP for the one-dimensional blood flow equations assuming subcritical flow. To the authors' knowledge, the complete solution of the J-CRP considering all possible wave-patterns is not available. This implies that we cannot handle supercritical and transcritical flows at junctions, which might be present in physiological situations due to vein collapse with discontinuous parameters in the human body, see [58]. For the solution of the CRP for subcritical flows with discontinuous material properties for blood flow with $n = 0$ and $m > 0$ refer to [59], and to [47] with $n < 0$ and $m > 0$. For arteries, [60,61] solved in complete detail the CRP with discontinuous material properties. For the solution of the J-CRP in blood flow for subcritical flows with $n < 0$ and $m > 0$, see also [44]. See [24–26,43] for the solution of the J-CRP using a more geometrical approach and for general conservation laws.

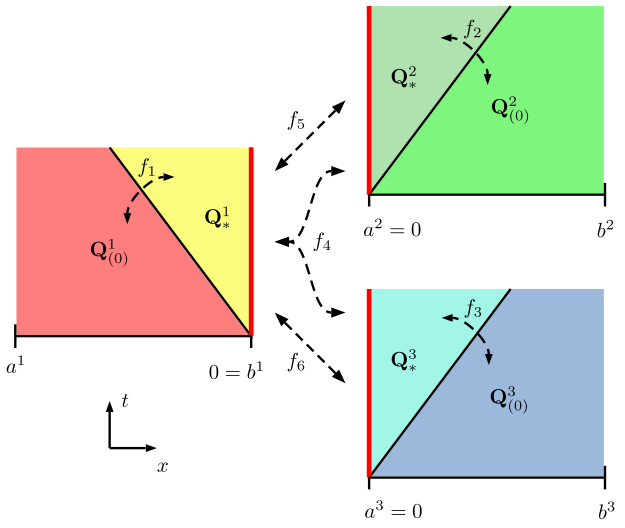

Fig. 2. Representation of a J-CRP for a typical 2×2 non-linear system with $N = 3$ vessels, where $b^1 = 0$, $a^2 = 0$ and $a^3 = 0$ are the local coordinates of vertex V for the first, second and third vessel respectively. The non-linear function f_k connects the initial condition $\mathbf{Q}^k_{(0)}$ and unknown $\mathbf{Q}^k_*$ for $k = 1 \dots, 3$, f_4 connects all the unknowns $\mathbf{Q}^1_*, \mathbf{Q}^2_*, \mathbf{Q}^3_*$, while f_5 and f_6 connect the unknown $\mathbf{Q}^1_*$ to $\mathbf{Q}^2_*$ and $\mathbf{Q}^3_*$, respectively.

The coupling conditions that connect states $\mathbf{Q}^k_*$, with $k = 1, \dots, N$, among themselves are

$$\mathbf{\Phi}(\mathbf{Q}^1_*, \dots, \mathbf{Q}^N_*) = \begin{bmatrix} \sum_{k=1}^{N} g^k A^k_* u^k_* \\ p_t(A^1_*, u^1_*; K^1, A^1_0) - p_t(A^2_*, u^2_*; K^2, A^2_0) \\ \vdots \\ p_t(A^1_*, u^1_*; K^1, A^1_0) - p_t(A^N_*, u^N_*; K^N, A^N_0) \end{bmatrix} = \mathbf{0}\,, \tag{38}$$

where the vector of conserved variables $\mathbf{Q}$ is defined in (6), while K^k and A^k_0 are the material properties of the k-th vessel. The auxiliary function g^k indicates whether the k-th vessel has vertex V at a^k or b^k, and reads

$$g^k = \begin{cases} -1 & a^k = 0\,, \\ 1 & b^k = 0\,, \end{cases} \tag{39}$$

p_t denotes *total pressure*

$$p_t(A, u; K, A_0) = \frac{1}{2}\rho u^2 + p(A; K, A_0)\,, \tag{40}$$

and p is the pressure given in (2). The first component of $\mathbf{\Phi}$ assures conservation of mass, whereas all the remaining components, from the second to the N-th, guarantee equality of total pressure in all the vessels meeting at vertex V. Since the number of vectors $\mathbf{Q}^k_*$ is N and each vector has two components A^k_* and $q^k_* = A^k_* u^k_*$, the total number of unknowns is $2N$. This means that we need a total number of $2N$ equations to close the system. The coupling conditions $\mathbf{\Phi}$ contain N equations, while the other N equations are obtained by connecting each state $\mathbf{Q}^k_*$ to the initial condition $\mathbf{Q}^k_{(0)}$ through non-linear waves for $k = 1, \dots, N$. The total number of equations are $2N$ and therefore the system is closed. (See Fig. 2.)

The non-linear relationship between $\mathbf{Q}^k_*$ and $\mathbf{Q}^k_{(0)}$, with $k = 1, \dots, N$, reads

$$u^k_* - u^k_{(0)} + g^k \beta(A^k_*; A^k_{(0)}, K^k, A^k_0) = 0\,, \quad k = 1, \dots, N\,, \tag{41}$$

where the non-linear function β is

$$\beta(A_*; A, K, A_0) = \begin{cases} \displaystyle\int_A^{A_*} \frac{c(\tau; K, A_0)}{\tau} \mathrm{d}\tau & \text{if } A_* \le A\,, \quad \text{rarefaction wave,} \\ \displaystyle\sqrt{B(A_*; A, K, A_0)\frac{A_* - A}{A_* A}} & \text{if } A_* > A\,, \quad \text{shock wave.} \end{cases} \tag{42}$$

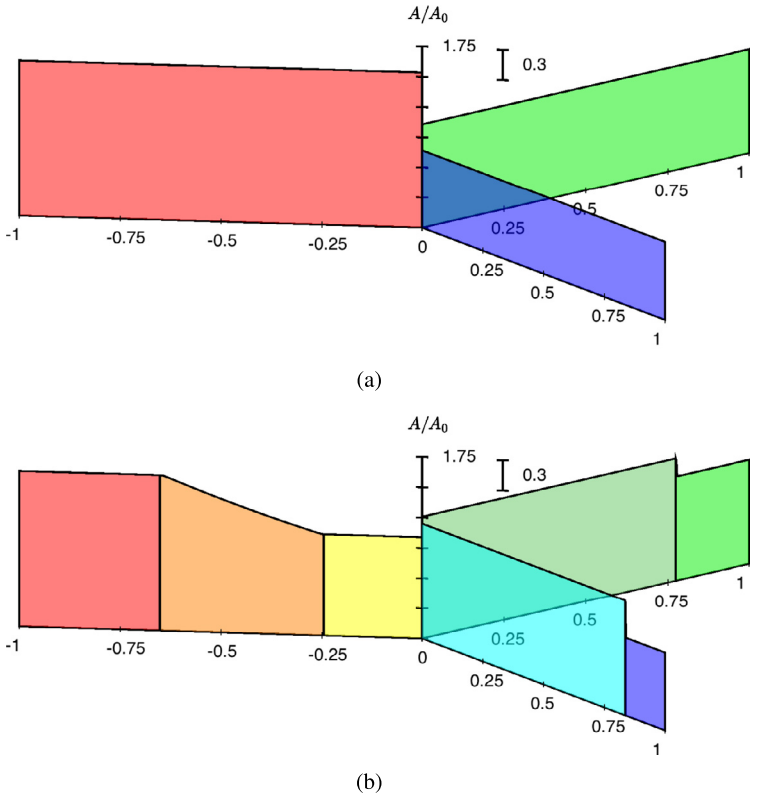

Fig. 3. Example of a J-CRP. Piece-wise constant data are given for each vessel. Frames (a) and (b) depict the solution at initial and output time for a simple J-CRP respectively. A rarefaction wave propagates backward in the left sub-domain, whereas two shocks move forward in the others.

The wave speed is

$$c(A;K,A_0)=\sqrt{\frac{K}{\rho}\left(m\left(\frac{A}{A_0}\right)^m-n\left(\frac{A}{A_0}\right)^n\right)}, \tag{43}$$

and the function B is

$$B(A_*;A,K,A_0)=\frac{K}{\rho}\left(\frac{m}{m+1}\frac{A_*^{m+1}-A^{m+1}}{A_0^m}-\frac{n}{n+1}\frac{A_*^{n+1}-A^{n+1}}{A_0^n}\right). \tag{44}$$

Gathering the information coming from Eqs. (38) and (41) we end up with the following

Proposition 2.1. *The solution of the J-CRP with N vessels for subcritical flow is found by solving the following non-linear system*

$$\left.\begin{aligned}
f_1(x_1,y_1;A^1_{(0)},u^1_{(0)}) &= y_1-u^1_{(0)}+g^1\beta(x_1;A^1_{(0)},K^1,A^1_0) &&=0\,,\\
&\vdots\\
f_N(x_N,y_N;A^N_{(0)},u^N_{(0)}) &= y_N-u^N_{(0)}+g^N\beta(x_N;A^N_{(0)},K^N,A^N_0) &&=0\,,\\
f_{N+1}(x_1,\dots,x_N,y_1,\dots,y_N) &= g^1x_1y_1+g^2x_2y_2+\cdots+g^Nx_Ny_N &&=0\,,\\
f_{N+2}(x_1,y_1,x_2,y_2) &= p_t(x_1,y_1;K^1,A^1_0)-p_t(x_2,y_2;K^2,A^2_0) &&=0\,,\\
&\vdots\\
f_{2N}(x_1,y_1,x_N,y_N) &= p_t(x_1,y_1;K^1,A^1_0)-p_t(x_N,y_N;K^N,A^N_0) &&=0\,,
\end{aligned}\right\} \tag{45}$$

where the unknowns of the problem are

$$\mathbf{X}=[x_1,\dots,x_N]=[A^1_*,\dots,A^N_*]\,,\quad \mathbf{Y}=[y_1,\dots,y_N]=[u^1_*,\dots,u^N_*]\,, \tag{46}$$

with β and p_t defined in (42) and (40), respectively.

The k-th non-linear function f_k connects the initial condition $\mathbf{Q}^k_{(0)}$ to the unknown $\mathbf{Q}^k_*$ for $k = 1, \dots, N$, f_{N+1} connects all the unknowns $\mathbf{Q}^1_*, \dots, \mathbf{Q}^N_*$, and f_{k+N} connects the unknown $\mathbf{Q}^1_*$ to the unknown $\mathbf{Q}^k_*$ for $k = 2, \dots, N$. We note that Proposition 2.1 is a generalization of Proposition 4.6 of [59]. A J-CRP solver for 2 vessels with different parameters K, A_0 corresponds to the CRP solver with piece-wise constant parameters K, A_0 for a single vessel. As we have assumed subcritical flow, then the Godunov states of problem of the J-CRP will be $\mathbf{D}^k(0) = \mathbf{Q}^k_*$ for $k = 1, \dots, N$. See Fig. 3 for an example of a J-CRP.

Sherwin et al. [62] solved the above system for blood flow assuming a two-rarefaction wave-pattern for the function β defined in (42), namely they assumed $A^* \leq A$. This hypothesis can be seen as an approximate J-CRP solver, through which numerical simulations show acceptable numerical results, see [62]. See also [44] for the first complete description of the solution of the J-CRP for blood flow, where both shocks and rarefaction waves are admitted for the genuinely non-linear characteristic fields.

2.4. A new implicit J-GRP solver

Here we propose a new implicit solver for the J-GRP. Following the idea of the explicit HEOC solver for the J-GRP proposed in [45] and the implicit MT-HEOC solver for the GRP in [42], we propose to combine them and construct the MT-HEOC solver for the J-GRP.

The J-GRP solutions along the t-axis $\mathbf{Q}^k_V(\tau)$, with $k = 1, \dots, N$, of (33) with coupling conditions $\mathbf{\Phi}$ are found by solving the following J-CRP at the vertex V with N vessels and coupling conditions $\mathbf{\Phi}$

$$\left.\begin{array}{ll} \text{PDEs:} & \partial_t \mathbf{Q}^k + \partial_x \mathbf{F}(\mathbf{Q}^k) = \mathbf{0}\,, \quad x \in I_k = \left(a^k, b^k\right), \quad t > 0\,, \\ \text{ICs:} & \mathbf{Q}^k(x,0) = \hat{\mathbf{Q}}^k_{(0)}(\tau)\,, \end{array}\right\} \quad k = 1, \dots, N\,, \tag{47}$$

where $\hat{\mathbf{Q}}^k_{(0)}(\tau)$, with $k = 1, \dots, N$, are constant vectors. The evolved values $\hat{\mathbf{Q}}^k_{(0)}(\tau)$ are found by applying for each k-th vessel the implicit Taylor expansion at the vertex V up to time τ, that is, by solving the following non-linear problem: find $\hat{\mathbf{U}}^k_{(0)}$ such that

$$\mathbf{L}(\hat{\mathbf{U}}^k_{(0)}; \mathbf{U}^k_{(0)}, \tau) = \mathbf{0}\,, \tag{48}$$

where the leading term $\mathbf{U}^k_{(0)}$ is

$$\mathbf{U}^k_{(0)} = [\mathbf{U}^{k,0}_{(0)}, \dots, \mathbf{U}^{k,M}_{(0)}]\,, \quad \mathbf{U}^{k,j}_{(0)} = \begin{cases} \partial^{(j)}_x \mathbf{Q}^k_{(0)}(0_+) = \lim_{x \to 0_+} \partial^{(j)}_x \mathbf{Q}^k_{(0)}(x)\,, & \text{if } a^k = 0\,, \\ \partial^{(j)}_x \mathbf{Q}^k_{(0)}(0_-) = \lim_{x \to 0_-} \partial^{(j)}_x \mathbf{Q}^k_{(0)}(x)\,, & \text{if } b^k = 0\,, \end{cases} \quad j = 0, \dots, M\,. \tag{49}$$

The solution procedure of the non-linear problems (48) is termed here the *evolution stage*. As in the MT-HEOC solver for the GRP, a possible initial guess for a numerical method to find solution of the non-linear problem (48) is $\mathbf{U}^k_{(0)}$. Once we solve problem (48), then the evolved vector $\hat{\mathbf{Q}}^k_{(0)}(\tau)$ will be the first entry of $\hat{\mathbf{U}}^k_{(0)}$, namely $\hat{\mathbf{U}}^{k,0}_{(0)}$. The sought J-GRP solutions along the t-axis at time $t = \tau$ are the Godunov states of the J-CRP (47) with initial data $\hat{\mathbf{Q}}^k_{(0)}(\tau)$, with $k = 1, \dots, N$, and self-similar solutions $\mathbf{D}^k(x/t)$, namely

$$\mathbf{Q}^k_V(\tau) = \mathbf{D}^k(0)\,, \quad k = 1, \dots, N\,. \tag{50}$$

Assuming subcritical flow, the values $\mathbf{Q}^k_V(\tau)$ are the N states $\mathbf{Q}^k_*$ described in Section 2.3.1, namely

$$\mathbf{Q}^k_V(\tau) = \mathbf{Q}^k_*\,, \quad k = 1, \dots, N\,. \tag{51}$$

We call the present method the MT-HEOC solver for the J-GRP, which extends the MT-HEOC solver for the GRP to the J-GRP. In the evolution stage of the MT-HEOC solver for the GRP, one applies an implicit Taylor series expansion to the left and right boundary extrapolated values, up to time $t = \tau$; this part gives left and right evolved values that are the initial conditions for a CRP. The solution along the t-axis of the GRP at time $t = \tau$ is then the Godunov state of the CRP. The natural generalization of the evolution stage of the MT-HEOC solver for the J-GRP is to apply an implicit Taylor series expansion on each vessel at the vertex V up to time $t = \tau$; this part gives evolved values that are the initial conditions for a J-CRP. The solutions along the t-axis of the J-GRP at time $t = \tau$ are then the Godunov states of a J-CRP.

See Fig. 4 for an illustration of the MT-HEOC solver for the J-GRP where we have $N = 3$ vessels. We use the implicit Taylor expansion to evolve the extrapolated values and find the evolved values $\hat{\mathbf{Q}}^1_{(0)}(\tau)$, $\hat{\mathbf{Q}}^2_{(0)}(\tau)$ and $\hat{\mathbf{Q}}^3_{(0)}(\tau)$. We then solve a J-CRP and find the solutions along the t-axis $\mathbf{Q}^1_V(\tau)$, $\mathbf{Q}^2_V(\tau)$ and $\mathbf{Q}^3_V(\tau)$.

We point out that our new method requires the solution of a non-linear problem for each k-th vessel with a total number of N non-linear problems of $m(M+1)$ unknowns, where N, m and M are respectively the total number of vessels, the number of components of the conserved variable $\mathbf{Q}$ and the order of the polynomials obtained by a reconstruction procedure. We remark that implicit solvers for the GRP and J-GRP are more costly than explicit ones and should only be used for problems that are known or suspected to be stiff.

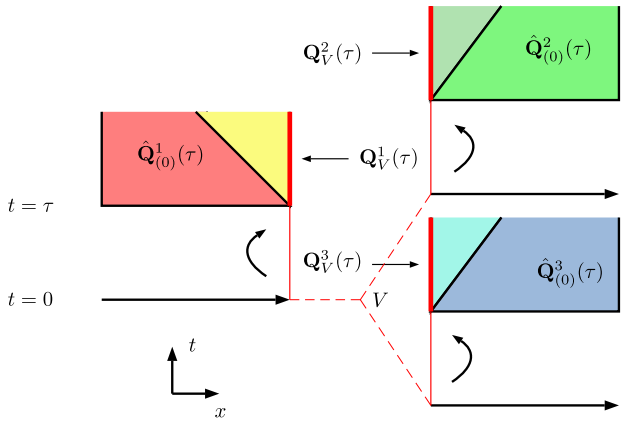

Fig. 4. Illustration of the MT-HEOC solver for the J-GRP with $N = 3$ vessels. The limiting values at vertex V are evolved separately up to time $t = \tau$. The sought solutions along the t-axis are the Godunov states of the J-CRP with these evolved states as initial data.

2.4.1. Spatial reconstruction

The spatial reconstruction is a crucial ingredient of the ADER finite volume methods. In the presence of boundaries, one has to take into account the lack of information given by the limited space. For instance, for a junction of three vessels, we do not have enough data to apply a classical three stencils WENO reconstruction [34] near the boundaries.

Borsche and Kall in [43] described a method that permits to fill the corresponding ghost cells using the information gained from the time derivatives of the Godunov states using either the Castro–Toro or the Toro–Titarev solver for the J-GRP. The same authors in [45] pointed out that in the explicit HEOC solver it is not possible to apply the same procedure as for the CT or the TT since we do not calculate the time derivatives of the Godunov states but rather directly evaluate the solutions of the J-GRP at time $t = \tau$. In the DET solver for the J-GRP, Müller and Blanco [44] proposed to fill the ghost cells using the spatial derivatives obtained from the implicit Discontinuous Galerkin prediction for solving the GRP. In this way, the inverse Cauchy–Kowalewskaya functionals used by Borsche and Kall [43] are avoided, and therefore the methodology can be applied to hyperbolic systems with non-invertible Jacobian matrices.

The MT-HEOC solver for the J-GRP gives more spatial information than its explicit version. In fact, by applying an implicit Taylor expansion, we evolve up to a certain time $t = \tau$ the extrapolated value of the reconstructed polynomial and its derivatives. Therefore, we should be able to apply the methodology proposed by Müller and Blanco [44]. As a matter of fact, the MT-HEOC solver replaces the numerical prediction of the DET solver with an implicit Taylor series expansion [42]. However, here we use a one-sided WENO reconstruction approach [63], following the HEOC solver in [45]. The drawback of using a one-sided WENO reconstruction, compared to the use of filled ghost cells, is the requirement of a minimum number of cells for each sub-domain. Indeed, to apply a k-th order scheme, we require at least k computational cells for each sub-domain.

2.4.2. Algorithm for evolving the solution in the complete network

Here we provide an algorithm to evolve the solution in the complete network, from time t^n to t^{n+1}, using a high-order ADER scheme with the MT-HEOC solver for both the J-GRP and the GRP. To approximate the time integrals of the junction-numerical fluxes in (35), we use the classical Gaussian quadrature rule with N_{Gauss} time quadrature points.

1. For each vertex V with N connected vessels, compute the junction-numerical fluxes located at the vertex V

$$\mathbf{F}^k_V = \frac{1}{\Delta t}\int_{t^n}^{t^{n+1}} \mathbf{F}(\mathbf{Q}^k_V(\tau))\mathrm{d}\tau \approx \sum_{h=1}^{N_{Gauss}} \omega_h \mathbf{F}(\mathbf{Q}^k_V(\tau_h)), \quad k = 1, \ldots, N, \tag{52}$$

applying the following procedure:

(a) for $k = 1, \ldots, N$ use a WENO one sided reconstruction procedure to obtain polynomials $\mathbf{Q}^k_{(0)}(x)$ at the junction interface;

(b) for $h = 1, \ldots, N_{Gauss}$

i. for $k = 1, \ldots, N$, apply an implicit Taylor expansion for each extrapolated value at the junction and find the evolved values $\hat{\mathbf{Q}}^k_{(0)}(\tau_h)$, as explained in Section 2.2.3;

ii. solve J-CRP (36) with initial data given by $\hat{\mathbf{Q}}^k_{(0)}(\tau_h)$ with $k = 1, \ldots, N$, as explained in Section 2.3.1 and find $\mathbf{Q}^k_V(\tau_h)$;

iii. for $k = 1, \ldots, N$ evaluate the quantity $\mathbf{F}(\mathbf{Q}^k_V(\tau_h))$;

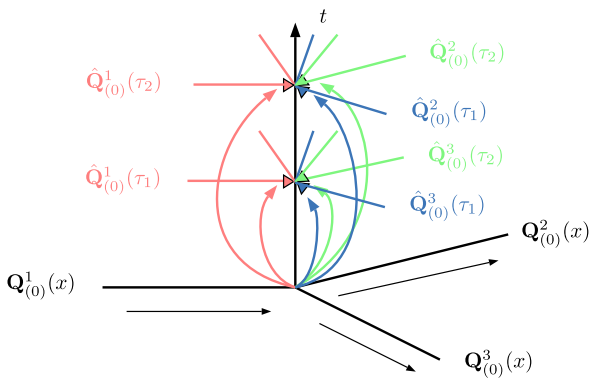

Fig. 5. Three-vessel J-GRP using the MT-HEOC solver. In this illustration we use $N_{Gauss} = 2$ Gaussian quadrature points. We evolve the limiting value at vertex V up to time τ_1 for each vessel, and then solve a J-CRP. The solutions along the t-axis are used to approximate the junction-numerical flux in (52) for each vessel. We repeat the procedure for time τ_2.

(c) For $k = 1, \ldots, N$ evaluate junction-numerical flux $\mathbf{F}^k_V$ in (52).

2. Apply a high-order ADER scheme to compute the numerical fluxes across interior cell interfaces and the numerical sources within the cells for each k-th vessel.
3. Update the solution from time t^n to t^{n+1} according with finite volume formula (11) for each k-th vessel.

See Fig. 5 for an illustration of step 1(b) of the proposed algorithm, which has advantages and disadvantages. As pointed out in Section 2.4.1, the main disadvantage is the lack of information needed to assign to the ghost cells outside the computational domain of each vessel. This can be overcome using a one-sided WENO reconstruction [63]. The main advantage in a HEOC-type scheme is having to solve just two types of non-linear problems: one for the evolution stage and another for the interaction of the evolved states through the J-CRP. As noted by Borsche and Kall [45], a HEOC-type solver is easier to implement, as compared to one proposed earlier [43]. It is worth noting that the ability of the present J-GRP solver to handle supercritical flows depends on that of its underlying J-CRP solver. Therefore, as long as we use a J-CRP that assumes subcritical flows, we will be unable to deal with trans and supercritical flows in networks.

3. Results

In this section we thoroughly assess the performance of the proposed methods. First, we perform an empirical convergence rate study of the proposed methods for a network of vessels with a single junction. Then, we assess the performance for a problem with stiff a source term. As a final test, we apply our mathematical model and described numerical method to the physical model of [46] that consists of a network of 37 compliant silicon tubes (arteries) and 21 junctions. In the following, we shall refer to the solver of the J-GRP proposed by Borsche and Kall [43] as the Borsche–Kall (BK) solver. Throughout this section, we shall also consider fully or partially high-order ADER methods. By *fully* high order we mean applying a high-order ADER method within the domain coupled to a high-order numerical approximation at junctions. By *partially* high order we mean applying a high-order ADER method within the domain coupled to a first-order numerical approximation at junctions.

3.1. Empirical convergence rate studies

To assess the order of convergence of the ADER scheme with the MT-HEOC solver for both the J-GRP and the GRP when solving balance laws in networks of vessels, we designed a test which is highly sensitive to the numerical treatment of the J-GRP. From this test, we expect the order of the method to depend on the order of the approximation of the junction-numerical fluxes. For instance, using a fifth-order solver within the domain, that is, a fifth-order solver for the numerical fluxes across interior cell interfaces and for the numerical sources within each cell, and a first-order solver for the junction-numerical fluxes, we expect the global error of the method to be of order one.

Here we manufactured a problem with exact solution by prescribing the following smooth vector-valued function

$$\tilde{\mathbf{Q}}(x,t) = \begin{bmatrix} A(x,t) \\ A(x,t)u(x,t) \end{bmatrix} = \begin{bmatrix} \tilde{A} + \tilde{a}\sin(\frac{2\pi}{L}x + \phi)\cos(\frac{2\pi}{T_0}t) \\ 0 \end{bmatrix}. \tag{53}$$

Then, inserting it in (5), we obtained a modified non-linear system

$$\partial_t \tilde{\mathbf{Q}} + \partial_x \mathbf{F}(\tilde{\mathbf{Q}}, x) - \mathbf{S}(\tilde{\mathbf{Q}}, x) = \tilde{\mathbf{S}}(\tilde{\mathbf{Q}}, x, t)\,, \tag{54}$$

for which $\tilde{\mathbf{Q}}(x,t)$ is the exact smooth solution, and the explicit formula for $\tilde{\mathbf{S}}(\mathbf{Q}, x, t)$ can be calculated by using a symbolic manipulator. The prescribed function $A(x,t)$ in (53) is product of trigonometric functions, periodic in time and space with

Table 1
Convergence rates study. The left column shows the various combinations of schemes used, the second column shows the meshes defined by the number of cells, the third to fifth columns show different GRP and J-GRP. For column TT-BK we show the L_∞ errors, the L_∞ order and the correspondent computational times in seconds; likewise for HEOC and the MT-HEOC. All numerical simulations were performed in an Intel Core i7-2600 with 4 cores (3.40 GHz clock speed). The code was not parallelized for these simulations. The order is spoiled when we use a first-order method at the junction.

Scheme	Cells	TT-BK			HEOC			MT-HEOC		
		E_∞	O_∞	t_{CPU} [s]	E_∞	O_∞	t_{CPU} [s]	E_∞	O_∞	t_{CPU} [s]
ADER1-J1	10	5.1069e−06		0.004	5.1069e−06		0.004	5.1069e−06		0.006
	20	3.2013e−06	0.6738	0.007	3.2013e−06	0.6738	0.009	3.2013e−06	0.6738	0.012
	40	1.7717e−06	0.8535	0.021	1.7717e−06	0.8535	0.020	1.7717e−06	0.8535	0.020
	80	9.2545e−07	0.9369	0.071	9.2545e−07	0.9369	0.072	9.2545e−07	0.9369	0.074
ADER2-J2	10	5.4495e−07		0.011	5.0373e−07		0.010	5.1298e−07		0.019
	20	1.6146e−07	1.7549	0.015	1.6387e−07	1.6201	0.016	1.6506e−07	1.6359	0.038
	40	4.3208e−08	1.9018	0.039	4.3361e−08	1.9181	0.047	4.3429e−08	1.9263	0.134
	80	1.1546e−08	1.9039	0.143	1.1558e−08	1.9075	0.172	1.1544e−08	1.9116	0.521
ADER3-J3	10	1.5862e−07		0.017	1.5711e−07		0.017	1.5346e−07		0.103
	20	1.5786e−08	3.3289	0.029	1.5482e−08	3.3431	0.034	1.4565e−08	3.3973	0.285
	40	1.7507e−09	3.1727	0.095	1.7299e−09	3.1618	0.122	1.6508e−09	3.1413	0.926
	80	2.2162e−10	2.9817	0.362	2.2288e−10	2.9564	0.464	2.1449e−10	2.9442	3.117
ADER4-J4	10	5.8856e−08		0.017	5.5043e−08		0.017	6.7511e−08		0.416
	20	5.8862e−09	3.3218	0.044	5.8208e−09	3.2413	0.051	5.9532e−09	3.5034	1.343
	40	3.1375e−10	4.2296	0.154	3.1273e−10	4.2182	0.187	3.1478e−10	4.2413	4.209
	80	2.6169e−11	3.5837	0.585	2.6156e−11	3.5797	0.725	2.6347e−11	3.5786	14.342
ADER5-J5	10	5.4857e−08		0.085	5.0963e−08		0.105	3.5734e−08		5.872
	20	1.2590e−09	5.4453	0.281	1.2550e−09	5.3437	0.349	1.2410e−09	4.8477	19.642
	40	2.0719e−11	5.9252	1.083	2.0704e−11	5.9217	1.340	2.0814e−11	5.8978	65.940
	80	5.7770e−13	5.1645	4.242	5.7776e−13	5.1633	5.261	5.0423e−13	5.3673	243.375
ADER2-J1	10	3.5206e−06		0.009	3.4324e−06		0.011	3.4821e−06		0.021
	20	1.6697e−06	1.0762	0.014	1.6639e−06	1.0447	0.020	1.6657e−06	1.0638	0.035
	40	8.0363e−07	1.0550	0.037	8.0313e−07	1.0509	0.045	8.0332e−07	1.0521	0.132
	80	3.9097e−07	1.0395	0.142	3.9092e−07	1.0388	0.166	3.9081e−07	1.0395	0.519
ADER3-J1	10	2.7055e−06		0.014	2.6961e−06		0.018	2.9330e−06		0.104
	20	1.5264e−06	0.8257	0.025	1.5261e−06	0.8210	0.032	1.5561e−06	0.9145	0.287
	40	7.7481e−07	0.9782	0.093	7.7475e−07	0.9781	0.120	7.7862e−07	0.9989	0.947
	80	3.8670e−07	1.0026	0.360	3.8668e−07	1.0026	0.467	3.8719e−07	1.0079	3.140
ADER4-J1	10	2.5458e−06		0.020	2.5457e−06		0.018	2.5619e−06		0.400
	20	1.5196e−06	0.7444	0.041	1.5195e−06	0.7444	0.050	1.5187e−06	0.7544	1.365
	40	7.8148e−07	0.9595	0.146	7.8144e−07	0.9594	0.186	7.8118e−07	0.9591	4.385
	80	3.9079e−07	0.9998	0.575	3.9079e−07	0.9998	0.727	3.9072e−07	0.9995	15.030
ADER5-J1	10	2.5562e−06		0.085	2.5544e−06		0.102	2.5320e−06		6.151
	20	1.5317e−06	0.7389	0.278	1.5315e−06	0.7381	0.359	1.5322e−06	0.7247	20.685
	40	7.8625e−07	0.9620	1.076	7.8618e−07	0.9620	1.341	7.8642e−07	0.9622	72.496
	80	3.9326e−07	0.9995	4.214	3.9324e−07	0.9995	5.249	3.9330e−07	0.9996	259.115

period T_0 and L respectively, and smooth at the junction, namely it satisfies $\partial_x^{(j)} A(0,t) = \partial_x^{(j)} A(L,t)$ with $j = 0, \dots, M$ for any time. Moreover, as $A(0,t) = A(L,t) = \tilde{A}$ and $u(0,t) = u(L,t) = 0$, the prescribed functions $A(x,t)$ and $u(x,t)$ satisfy the coupling conditions $\mathbf{\Phi}$ for blood flow (38) for $t \geq 0$.

The empirical convergence rate test was performed on a network of $N = 3$ vessels with one junction. We considered the three vessels with local coordinate $[a^1, b^1] = [-1, 0]$, and $[a^2, b^2] = [a^3, b^3] = [0, 1]$, and vertex V located in 0. The initial condition for the numerical test was given by the described function $\tilde{\mathbf{Q}}(x,t)$ at time $t = 0$. We considered constant parameters K, A_0, external pressure $p_e = 0$ and friction resistance $f = 0$, so that the source term $\mathbf{S}(\mathbf{Q}, x)$ was set to zero. Since the prescribed function $A(x,t)$ in (53) is periodic in space, we used periodic boundary conditions away from the junction. Vessel parameters are: $m = 1/2$, $n = 0$, cross-sectional radius at equilibrium $r_0 = 10$ mm, cross-sectional area at equilibrium $A_0 = \pi r_0^2$, Young modulus $E = 0.4$ MPa, wall-thickness at equilibrium $h_0 = 1.1$ mm, length $L = 1$ m. Computation parameters are: $T_0 = 1$ s, $\tilde{A} = A_0$, $\tilde{a} = 0.1 A_0$, $\phi = \frac{\pi}{2}$, output time $t_{end} = 0.5$ s, Courant number coefficient $CFL = 0.9$. Since the three vessels have the same material properties and computation parameters, the smoothness at the junction of the prescribed function $A(x,t)$ is assured. We compared results given by the TT and the BK solver for the GRP and the J-GRP respectively, the HEOC and the MT-HEOC solver for both the GRP and the J-GRP. We used the HLL [56] method to compute the numerical fluxes within each vessels, instead of solving exactly the CRP.

Table 1 shows empirical convergence rates for schemes of first to fifth accuracy in space and time. The first column of Table 1 shows the various combinations of schemes used, the second column shows the meshes defined by the number of cells, the third to fifth columns show different GRP and J-GRP. For column TT-BK, we show the L_∞ errors, the L_∞ order and

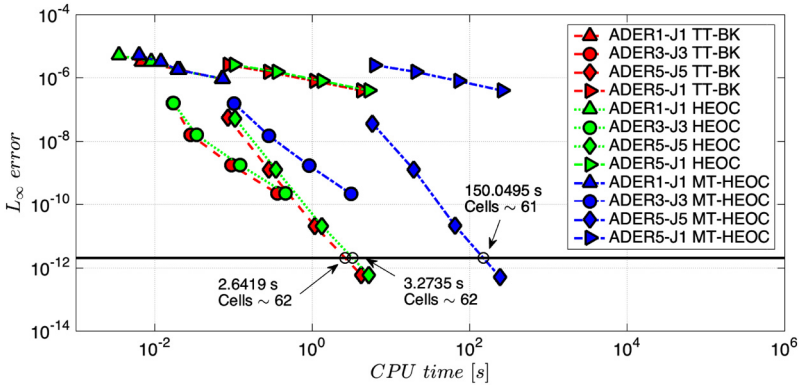

Fig. 6. Efficiency plot: L_∞ errors against computational times. Comparison between first, third and fifth-order ADER schemes with TT-BK, HEOC and MT-HEOC solvers for GRP and J-GRP is shown. Results for the fifth-order ADER scheme in the interior of the domain with a first-order scheme at the junction are also shown. Numerical results were obtained with meshes of $10, 20, 40, 80$ cells. The intersections between the horizontal line $E = 2 \times 10^{-12}$ (prescribed error) and the fifth-order ADER schemes give the computational times and number of cells required to attain the prescribed error E. For a color version of this figure, the reader is referred to the web version of this article.

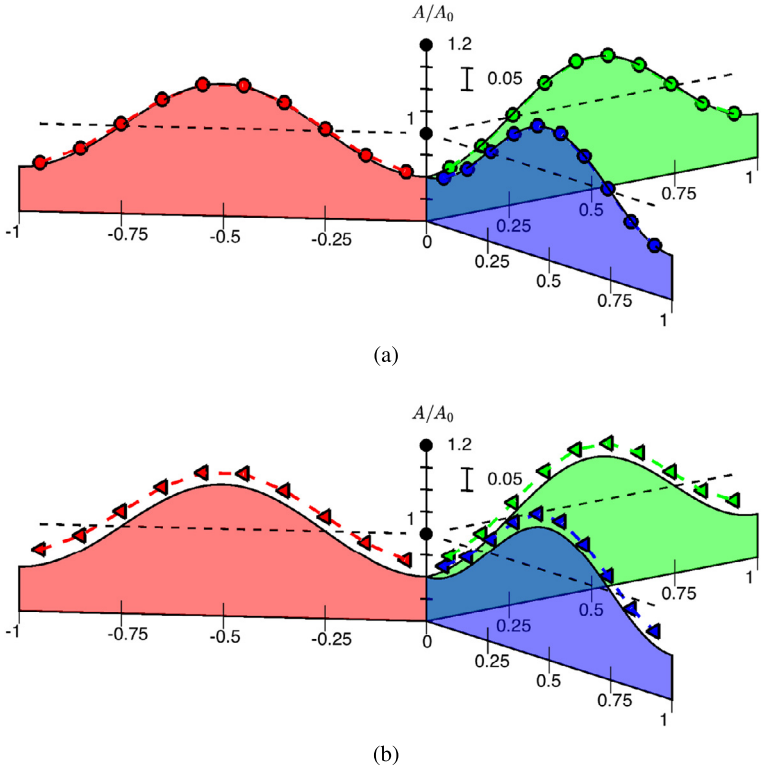

Fig. 7. Illustration of the empirical convergence rate study. The normalized cross-sectional area $\frac{A}{A_0}$ is depicted in the z variable. The dotted and the shaded plot depict the numerical and the exact solution respectively. We used 10 cells for each vessel and we stopped the simulation after 100.5 s. The ADER scheme with the MT-HEOC solver was used. Frame (a): numerical solution obtained by the fully third-order scheme. Frame (b): numerical solution obtained by the partially third-order scheme.

the computational times in seconds; likewise for HEOC and the MT-HEOC. Orders from one to five are attained as desired. It is worth noting two points. First, the order of accuracy in space and time is spoiled whenever we use a first-order approximation of the junction-numerical fluxes. For instance, when we use the combination ADER5-J1 with any of the solvers presented in Table 1, the accuracy decreases from five to one; likewise with other combinations. Therefore, even though we use a high-order scheme within each sub-domain but a first-order approximation of the junction-numerical fluxes, the overall accuracy in space–time is ruined. This means that low-order errors travel through the network when low-order schemes are used at junctions. Second, the implicit Taylor series expansion plays an important role in the computational cost. Indeed, there is a difference in the computational times between the numerical results obtained by using the explicit solvers TT-BK and HEOC, and the implicit solver MT-HEOC.

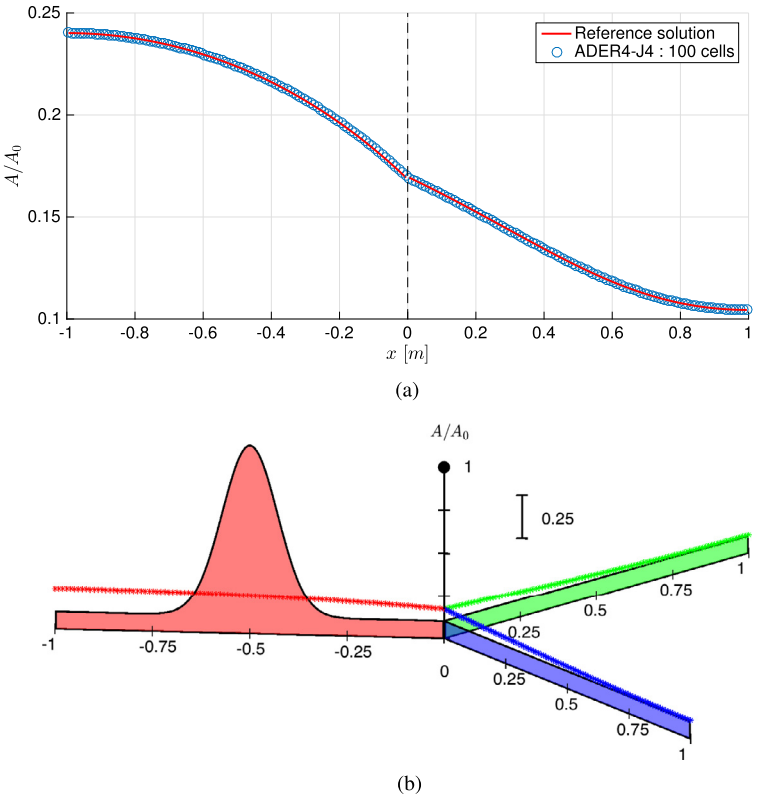

Fig. 8. A stiff problem connecting three vessels at a single junction. The fourth-order ADER scheme with the MT-HEOC solver for both the GRP and J-GRP was used. Frame (a): the normalized cross-sectional area $\frac{A}{A_0}$ at the fixed time $t_{end} = 2$ s as a function of axial distance is depicted for each vessel. Note that the vertical line at $x = 0$ represents the junction position. The normalized cross-sectional area of one vessel is depicted in $[-1, 0]$, while the remaining two are coincident and are depicted in $[0, 1]$. The numerical solution with 100 cells for each vessel is shown by ○, while a reference solution computed with a first-order method using 2000 cells for each vessel is shown by ——. Frame (b): illustration of the initial condition and computed results. The initial condition is depicted by the shaded graph, while the solution at the output time is shown by the single lines.

Fig. 6 depicts L_∞ errors against computational times. Comparison between first, third and fifth-order ADER schemes with TT-BK, HEOC and MT-HEOC solvers for GRP and J-GRP are shown. Also shown are results for the fifth-order ADER scheme in the interior of the domain with a first-order scheme at the junction. For the computation we used meshes of $10, 20, 40, 80$ cells. The point of this figure is to assess the performance of the schemes by relating the error to the computational cost. For example, prescribing the error $E = 2 \times 10^{-12}$, the computational times needed for the ADER scheme to attain that specific error are 2.6419 s, 3.2735 s and 150.0495 s using respectively the TT-BK, HEOC and the MT-HEOC solvers. Note that a first-order method would have attained that error at the computational time of ∼130 years; such figure is obtained by extrapolation, which is probably an underestimate. These observations support the use of high-order methods for hyperbolic balance laws, when small errors are aimed for. The results also show that the combination ADER5-J1 completely ruins the accuracy while maintaining the computational cost given by a fifth-order method. This suggests that the time to attain the above-mentioned error with a partially high-order method is even larger than that of a first-order method throughout. For instance, ADER5-J1 with the implicit MT-HEOC solver would have attained that error at the computational time of ∼98 *centuries*.

Fig. 7 depicts the normalized cross-sectional area $\frac{A}{A_0}$ for the exact solutions (shaded plot) and the numerical solutions (dotted line) for the three vessels at the output time. Frames (a) and (b) depict the numerical solutions from the fully and partially third-order ADER scheme with the MT-HEOC solver, respectively. The results show that a first order at the junction spoils the accuracy throughout the space–time domain.

From the empirical convergence rate studies, we conclude that it is imperative to use high-order numerical schemes at junctions, in order to preserve the desired high-order of accuracy in the full computational domain.

3.2. A stiff problem for a junction

Following the work of Müller et al. [64], we say that a source term is stiff when

$$\Delta x \frac{\max_i \left(|\beta_i|\right)}{\max_i \left(|\lambda_i|\right)} > 1 \,, \tag{55}$$

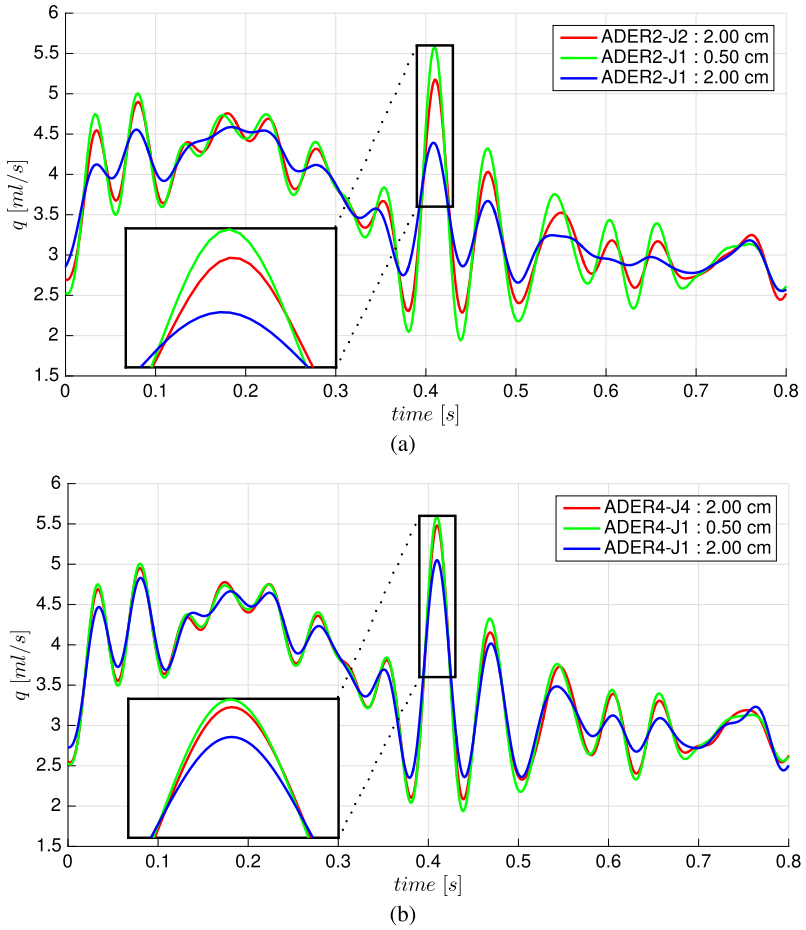

Fig. 9. Computed flow $q(x,t)$ at midpoint of left renal artery. The ADER scheme with the MT-HEOC solver for both the GRP and J-GRP was used. Frame (a): comparison between fully and partially second-order methods with different mesh sizes. Frame (b): comparison between fully and partially fourth-order methods with different mesh sizes. For a color version of this figure, the reader is referred to the web version of this article.

where Δx, β_i and λ_i are the spatial mesh size, the i-th eigenvalue of the Jacobian of the source term $\frac{\partial \mathbf{S}(\mathbf{Q})}{\partial \mathbf{Q}}$ and of the physical flux $\frac{\partial \mathbf{F}(\mathbf{Q})}{\partial \mathbf{Q}}$ respectively, see also [40]. In the one-dimensional blood flow equations, assuming constant parameters and zero external pressure, source term (7) reads

$$\mathbf{S}(\mathbf{Q}) = \begin{bmatrix} 0 \\ -R\frac{q}{A} \end{bmatrix}, \tag{56}$$

where $R = \gamma\pi\frac{\mu}{\rho}$. The eigenvalues of (56) are $\beta_1 = 0$ and $\beta_2 = -\frac{R}{A}$. Condition (55) can be written as

$$\Delta x \frac{R}{A \max_i(|\lambda_i|)} > 1\,. \tag{57}$$

As pointed out by Müller et al. [64], source term (56) may become stiff under physiological conditions. If the cross-sectional area A approaches zero, then ratio (57) increases arbitrarily leading to a stiff problem. This happens routinely in veins: they are highly compliant and collapse easily under physiological situations.

To test the capability of the ADER scheme with the MT-HEOC solver for both the GRP and the J-GRP to deal with stiff source terms, we considered a network of $N = 3$ arteries with one junction. Although arteries do not collapse under physiological conditions because they are stiffer and designed to endure high pressure from the pumping action of the heart, we could still simulate a problem in the stiff regime assuming condition (57) and appropriately adjusting the cross-sectional area of the initial condition.

We considered three vessels with local coordinate $[a^1, b^1] = [-1, 0]$, and $[a^2, b^2] = [a^3, b^3] = [0, 1]$, and vertex V located in 0. The initial condition for the cross-sectional area A for the first vessel was

$$A(x,0) = 0.1A_0 + A_0 e^{-100(x-0.5)^2}\,, \tag{58}$$

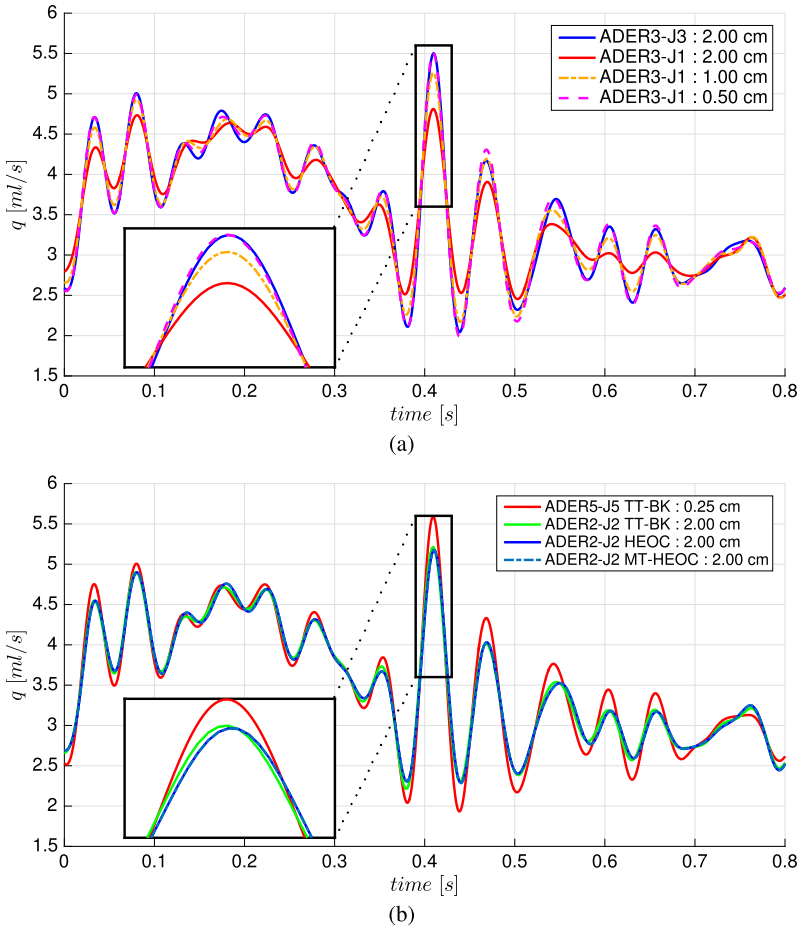

Fig. 10. Computed flow $q(x,t)$ at midpoint of left renal artery. Frame (a): the ADER scheme with the MT-HEOC solver for both the GRP and J-GRP was used. Comparison between fully and partially third-order methods with different mesh sizes. Frame (b): comparison between fully second-order schemes with different solvers, with a fixed mesh size. A reference solution is also shown (ADER5-J5 TT-BK: 0.25 cm). For a color version of this figure, the reader is referred to the web version of this article.

while for the other vessels was $A(x,0) = 0.1A_0$. Frame 8(b) shows $A(x,0)$ in the three vessels at the initial time. For each vessel we set $u(x,0) = 0$. Vessels parameters are: $m = 1/2$, $n = 0$, length $L = 1$ m, cross-sectional radius at equilibrium $r_0 = 0.1$ mm, cross-sectional area at equilibrium $A_0 = \pi r_0^2$, Young modulus $E = 0.4$ MPa, wall-thickness at equilibrium $h_0 = 1.1$ mm, resistance defined in (56) $R = 8\pi\frac{\mu}{\rho}$ and dynamic viscosity $\mu = 2.5$ mPa s. Computation parameters are: output time $t_{end} = 2$ s, 100 cells, Courant number coefficient $CFL = 0.9$. Transmissive boundary conditions were used away from the junction. With the given parameters, ratio (57) at the junction varies in time from 3 to 7 and results in a stiff problem.

Frame 8(a) shows computed results for a fourth-order ADER scheme with the MT-HEOC solver for both the GRP and J-GRP. Satisfactory agreement is seen between the computed solution ○ and a reference solution obtained with a first-order method with a fine grid of 2000 cells ——. See legend of 8(a) for further information. It is worth remarking that for this test problem, if one uses an explicit solver for the J-GRP, the simulation fails after few time steps. This observation emphasizes that in the stiff regime the use of a locally implicit solver is mandatory. See Frame 8(b) for an illustration of the initial condition and the computed results.

3.3. Application to a network of arteries

In this section, we consider the model network of major arteries presented by Matthys et al. [46], composed of 37 tubes that represent arteries, a pump that resembles the outflow of blood from the heart and terminal resistances. Mechanical properties of each vessel, terminal resistances, network geometry, and inflow measured at the root of ascending aorta are given in [46,11].

In the physical model of Matthys et al. [46], the cross-sectional area at equilibrium A_0 varies along the vessel length and this requires the use of well-balanced schemes. Non-well-balanced schemes may give wrong numerical results as pointed out in [65]. The current version of our scheme is not strictly well-balanced. Therefore, we have slightly modified the physical model of Matthys et al. [46] by neglecting the taper of tubes and taking mean values for parameters, for each vessel.

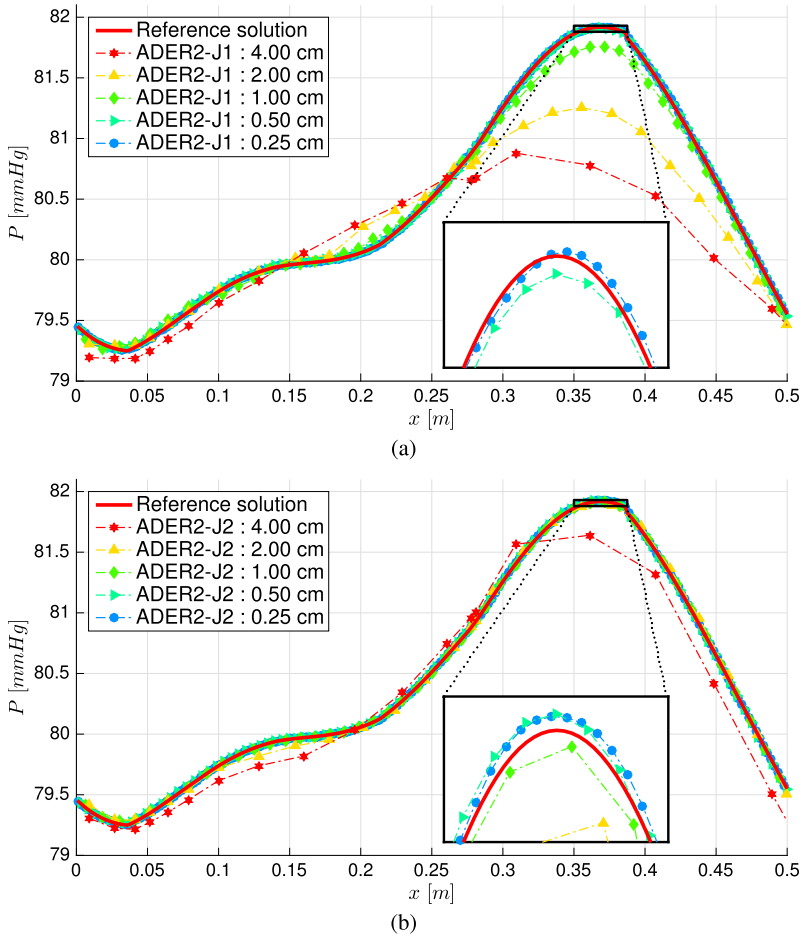

Fig. 11. Computed pressure along the aorta and part of the right iliac femoral (vessel nos. 1, 8, 10, 15, 17, 23, 25, 27, 28 of model in [46]). The fully and partially second-order ADER schemes with the MT-HEOC solver were used. Mesh size runs from 0.25 cm to 4 cm. A reference solution from a fully fifth-order ADER scheme with a mesh size of 0.125 cm is depicted. Frame (a): numerical results with a fully second-order method are shown. Frame (b): numerical results with a partially second-order method are shown.

Computations were performed using $CFL = 0.9$, the inflow boundary condition and terminal resistances were treated as in [11], and the tube law was purely elastic. The number of cells M_{cells} for each vessel was chosen according to

$$M_{cells} = max(floor(L/\Delta x_{max}), ord) \, , \tag{59}$$

where L is the length of the vessel, Δx_{max} is the maximal space size (e.g. 0.02 m) and ord is the order of the numerical method. Throughout the results we only refer, for instance, to 2 cm to indicate $\Delta x_{max} = 0.02$ m. Numerical results obtained with fully and partially high-order methods with the same order of accuracy, have the same spatial mesh size. Accordingly to the above-mentioned criterion, the mesh is different for each order of accuracy. Therefore, caution is required in assessing the numerical results obtained with different orders.

Another way to proceed with the assessment of results from high-order methods, in our case from one to five, is to impose a minimum number of cells which is common for all orders; in the present case the minimum is five. To do so we utilize the following procedure

$$M_{cells} = max(floor(L/\Delta x_{max}), 5) \, . \tag{60}$$

However there is a drawback with this approach. As the mesh is already fine enough, the differences between fully and partially high-order approximations are not clearly manifested in the results. In other words, the fine mesh has masked the high-order effect of the methods. Such phenomenon is more evident for the schemes in the high-order range. Throughout this paper, the default criterion is given by (59), unless specified.

Figs. 9 and 10 show the computed flow $q(x, t)$ of the left renal artery after 20 cardiac cycles and the maximum flow peak at cardiac reference time 0.4 s. For Fig. 9 and Frame 10(a), we used ADER methods of different orders, with the MT-HEOC solver. Frame 9(a) compares fully and partially second-order methods. A first-order method at junctions spoils the accuracy in space and time with a damping effect for extrema. The fully second-order method with 2 cm —— is

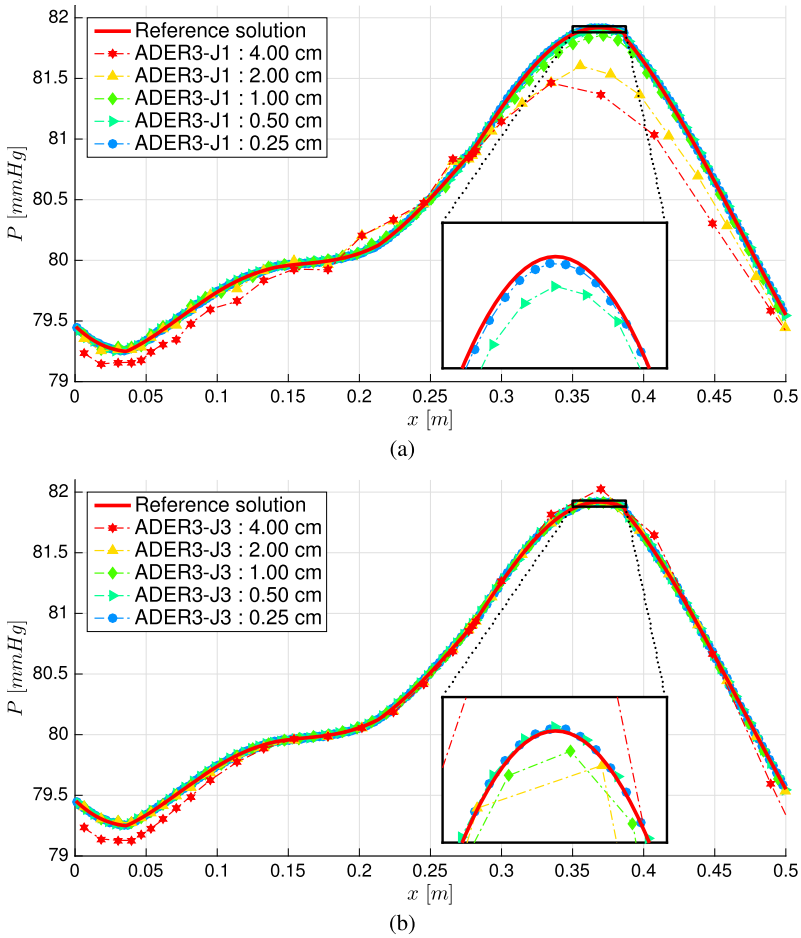

Fig. 12. Computed pressure along the aorta and part of the right iliac femoral (vessel nos. 1, 8, 10, 15, 17, 23, 25, 27, 28 of model in [46]). The fully and partially third-order ADER schemes with the MT-HEOC solver were used. Mesh size runs from 0.25 cm to 4 cm. A reference solution from a fully fifth-order ADER scheme with a mesh size of 0.125 cm is also depicted. Frame (a): numerical results with a fully third-order method are shown. Frame (b): numerical results with a partially third-order method are shown.

comparable with the partially second-order method with 0.5 cm ——. Similar results can be found for fully and partially fourth-order ADER methods in Frame 9(b). Fully and partially third-order methods with different mesh sizes can be found in 10(a). The partially third-order method requires a mesh size of 0.5 cm - - - to match the solution obtained with the fully third-order method with a mesh size of 2 cm ——, and the computational times per cardiac cycle are respectively 29.859 s and 9.556 s, see Table 2. The computational time of the partially third-order method is three times larger than the one of the fully third-order method. This observation emphasizes the better efficiency of high-order methods used at junctions. Frame 10(b) shows a comparison between different solvers. We compare the numerical results given by the TT-BK, the HEOC and the MT-HEOC solvers for the GRP and the J-GRP for a fixed mesh size of 2 cm. A reference solution given by the fifth-order ADER scheme with the TT-BK solver for the GRP and the J-GRP using a fine mesh size of 0.25 cm is also shown. All solvers give similar numerical results.

Figs. 11 to 14 depict computed pressure in the aorta and part of the right iliac femoral, at the output time. Numerical results were obtained using ADER schemes of different orders, with the MT-HEOC solver. In Fig. 14 the minimum number of cells was chosen accordingly to (60). A reference solution obtained using a fully fifth-order method with a fine mesh size of 0.125 cm is also shown. A first-order method at junctions spoils the accuracy of the numerical schemes insofar as first-order errors travel throughout the network of vessels with a damping effect for the pressure pulse-wave. Frames 11(a) and 11(b) show numerical results using fully and partially second-order methods, respectively. The second-order method at junctions improves the accuracy for pressure. A similar pattern is also seen with fully and partially third and fourth-order schemes; the numerical results are shown in Figs. 12 and 13, respectively. The fully second and the partially fourth-order solvers using a mesh size of 2 cm are comparable. Computational times per cardiac cycle are respectively 1.621 s and 33.373 s, see Table 2. The computational time of the partially fourth-order method is 20 times larger than that for the fully second-order method. This suggests that accurate numerical results with less computational effort can be achieved by using high-order numerical methods at junctions. Frames 14(a) and 14(b) show numerical results using fully and partially second-order

Table 2
Errors and computational times for a network of arteries. Left column shows the meshes defined by the maximum spatial mesh size Δx_{max}. Second to fourth columns show results different combinations of GRP and J-GRP solvers. Within every column we show L_1 errors and corresponding computational times for two combination of schemes. L_1 errors were evaluated considering the flows $q = Au$ in the whole arterial system; for a reference solution we used the fully fifth-order ADER scheme with a mesh size of 0.125 cm. All numerical simulations were performed in an Intel Core i7-2600 with 4 cores (3.40 GHz clock speed). The code was parallelized by means of *openMP*. Simulations were stopped after twenty cardiac cycles.

cm	TT-BK		TT		HEOC				MT-HEOC			
	L_1	t_{CPU} [s]	L_1	t_{CPU} [s]	L_1	t_{CPU} [s]	L_1	t_{CPU} [s]	L_1	t_{CPU} [s]	L_1	t_{CPU} [s]
	ADER2-J2		ADER2-J1		ADER2-J2		ADER2-J1		ADER2-J2		ADER2-J1	
4.00	1.9259e−06	13.62	2.7016e−06	8.13	2.3375e−06	13.28	2.7015e−06	8.94	2.3385e−06	22.47	2.7011e−06	17.24
2.00	8.4894e−07	18.18	2.0112e−06	11.21	9.3598e−07	15.48	2.0112e−06	12.26	9.3386e−07	32.42	2.0115e−06	26.47
1.00	2.5310e−07	21.33	1.2044e−06	15.89	2.6439e−07	22.52	1.2044e−06	18.49	2.6125e−07	49.84	1.2023e−06	44.85
0.50	6.4895e−08	33.37	2.6798e−07	27.30	6.6194e−08	37.56	2.6797e−07	33.73	6.9441e−08	91.83	2.6526e−07	86.72
0.25	1.6004e−08	145.51	8.3692e−08	125.89	1.6343e−08	156.73	8.3690e−08	149.62	4.8067e−08	415.60	9.7928e−08	400.10
	ADER3-J3		ADER3-J1		ADER3-J3		ADER3-J1		ADER3-J3		ADER3-J1	
4.00	1.1156e−06	29.80	2.4775e−06	20.35	9.0297e−07	35.73	2.4775e−06	22.22	9.0297e−07	121.02	2.4775e−06	102.87
2.00	3.8831e−07	41.32	1.8020e−06	30.23	3.2900e−07	45.01	1.8020e−06	34.55	3.2899e−07	191.12	1.8020e−06	174.09
1.00	1.7415e−07	58.48	8.7341e−07	48.69	1.8747e−07	70.16	8.7339e−07	58.08	1.8744e−07	333.59	8.7336e−07	313.27
0.50	4.3286e−08	99.71	2.4397e−07	90.38	4.3579e−08	119.12	2.4396e−07	107.56	4.3567e−08	624.63	2.4394e−07	597.18
0.25	1.4918e−08	305.94	6.1851e−08	291.07	1.5206e−08	348.90	6.1850e−08	335.37	1.5195e−08	1953.85	6.1819e−08	1942.40
	ADER4-J4		ADER4-J1		ADER4-J4		ADER4-J1		ADER4-J4		ADER4-J1	
4.00	8.4933e−07	50.16	2.1885e−06	33.67	1.1062e−06	56.95	2.1885e−06	39.30	1.1062e−06	442.74	2.1885e−06	433.08
2.00	2.8120e−07	69.17	1.4788e−06	54.67	2.1396e−07	73.79	1.4788e−06	57.55	2.1396e−07	687.75	1.4788e−06	667.46
1.00	1.0004e−07	99.75	7.0308e−07	83.25	6.5577e−08	113.54	7.0306e−07	97.97	6.5577e−08	1194.90	7.0306e−07	1194.90
0.50	3.3719e−08	170.22	2.3124e−07	154.05	2.5942e−08	203.87	2.3123e−07	189.50	2.5942e−08	2315.43	2.3123e−07	2348.78
0.25	1.4633e−08	398.09	5.4277e−08	389.10	1.4077e−08	459.91	5.4276e−08	439.69	1.4077e−08	5399.23	5.4276e−08	5431.68
	ADER5-J5		ADER5-J1		ADER5-J5		ADER5-J1		ADER5-J5		ADER5-J1	
4.00	4.1746e−07	119.61	1.8771e−06	88.18	7.6933e−07	143.58	1.8770e−06	106.82	7.6933e−07	3834.08	1.8770e−06	3693.50
2.00	2.7524e−07	162.53	1.3384e−06	121.84	2.3790e−07	179.39	1.3384e−06	153.56	2.3790e−07	5064.60	1.3384e−06	5161.99
1.00	9.4003e−08	241.21	6.6951e−07	211.75	9.5565e−08	283.49	6.6950e−07	255.51	9.5565e−08	8564.96	6.6950e−07	9097.09
0.50	3.1106e−08	439.28	2.2883e−07	412.24	2.9227e−08	520.58	2.2882e−07	492.50	2.9227e−08	15949.96	2.2882e−07	16603.64
0.25	1.4652e−08	862.57	5.3384e−08	778.46	1.4200e−08	953.31	5.3383e−08	927.03	1.4200e−08	29192.95	5.3383e−08	29246.10

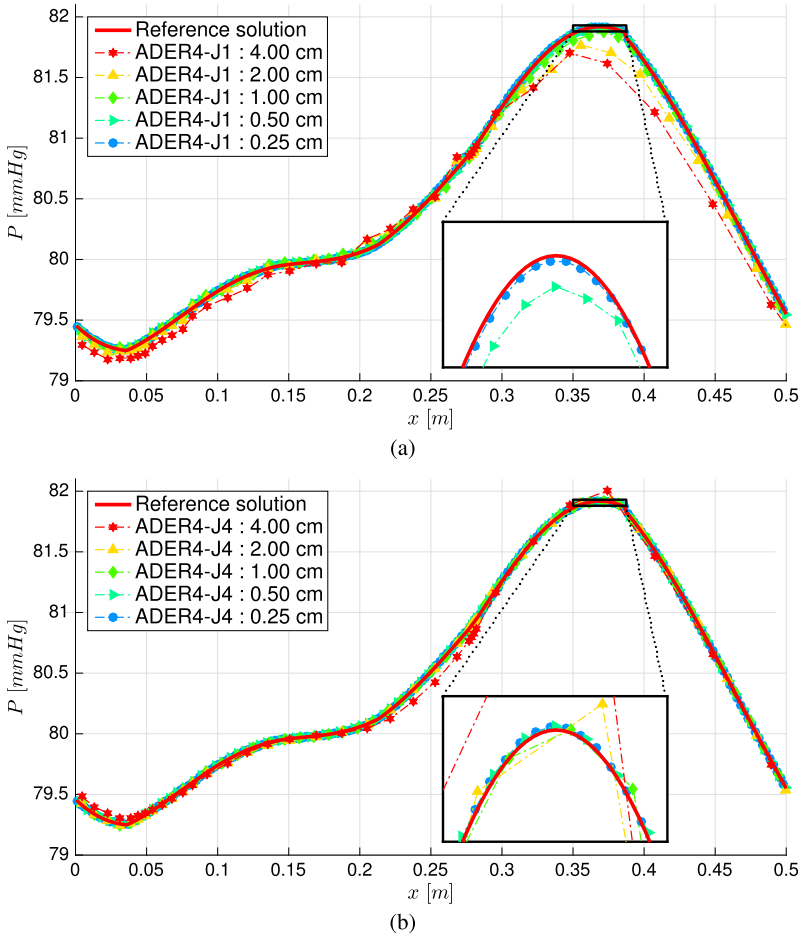

Fig. 13. Computed pressure along the aorta and part of the right iliac femoral (vessel nos. 1, 8, 10, 15, 17, 23, 25, 27, 28 of model in [46]). The fully and partially fourth-order ADER schemes with the MT-HEOC solver were used. Mesh size runs from 4 cm to 0.25 cm. A reference solution from a fully fifth-order ADER scheme with a mesh size of 0.125 cm is also depicted. Frame (a): numerical results with a fully fourth-order method are shown. Frame (b): numerical results with a partially fourth-order method are shown.

methods, respectively, where the minimum number of cells was 5. The numerical results are improved throughout. A second order method at junctions improves the accuracy for pressure, even though the differences are less significant than that depicted in Frames 11(a) and 11(b).

Table 2 shows L_1 errors and computational times for schemes of order up to five in space and time using different combination of solvers. First-order methods at junctions coupled with high-order methods in the interior of the domain have larger errors compared to fully high-order methods. Computational times for the implicit solver MT-HEOC are larger compared to the explicit ones.

Fig. 15 depicts L_1 errors against computational times. We compare ADER schemes of different orders, in all cases using the MT-HEOC solver. Errors of fully high-order methods (red-shaded colors) are always below to partially high-order methods (blue-shaded colors). It is worth noting that we formally do not preserve fully high-order accuracy in the whole arterial network due to our simple, low order, treatment of inflow boundary condition and terminal resistances. Consequently, the decreased rate of the fully fifth-order method is nearly equivalent to the fully second-order scheme. Nevertheless, the benefit of using high-order methods at junctions remains visible, but quite clearly, for a real application one must incorporate appropriate treatment of the inflow boundary and terminal resistances.

4. Summary and conclusions

Here we have proposed a new implicit solver for the Junction-Generalized Riemann Problem (J-GRP). This solver is an extension of the recently proposed Montecinos–Toro implicit solver for the GRP. We have then put together the two building blocks in the ADER framework to construct schemes of arbitrary accuracy in space and time for system of hyperbolic balance laws in networks. Specifically, we have applied the resulting methods to networks of blood vessels. To systematically assess convergence rates we have proposed a test problem with exact solution, consisting of three vessels connected at a single

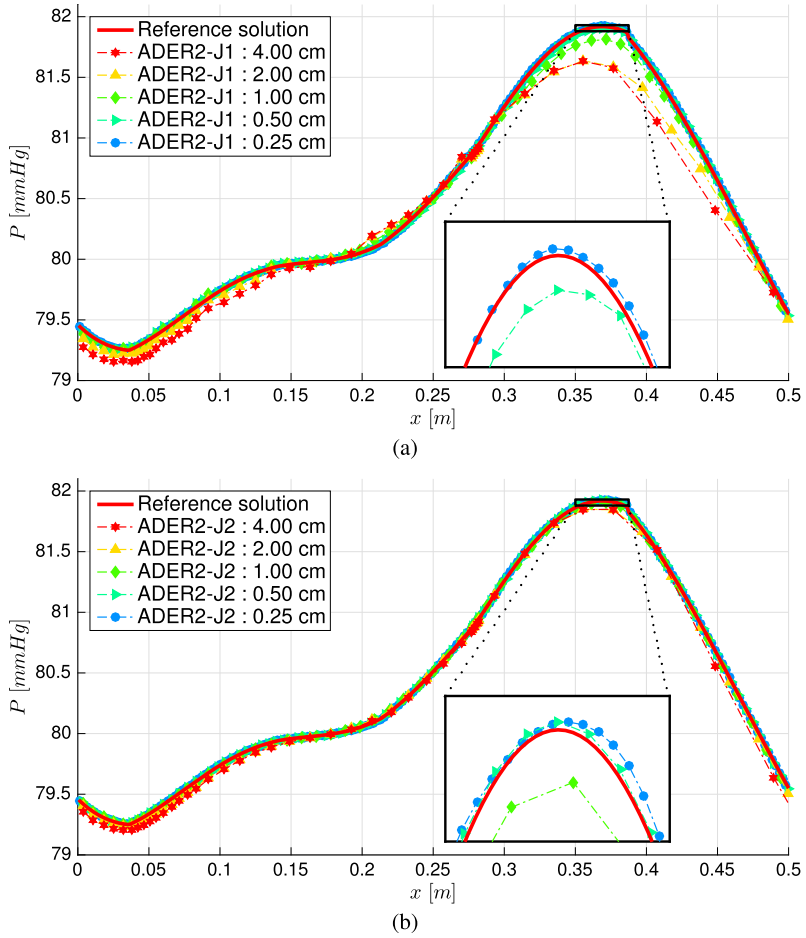

Fig. 14. Computed pressure along the aorta and part of the right iliac femoral (vessel nos. 1, 8, 10, 15, 17, 23, 25, 27, 28 of model in [46]). The fully and partially second-order ADER schemes with the MT-HEOC solver were used. Mesh size runs from 0.25 cm to 4 cm. The minimum number of cells was 5. A reference solution from a fully fifth-order ADER scheme with a mesh size of 0.125 cm is depicted. Frame (a): numerical results with a fully second-order method are shown. Frame (b): numerical results with a partially second-order method are shown.

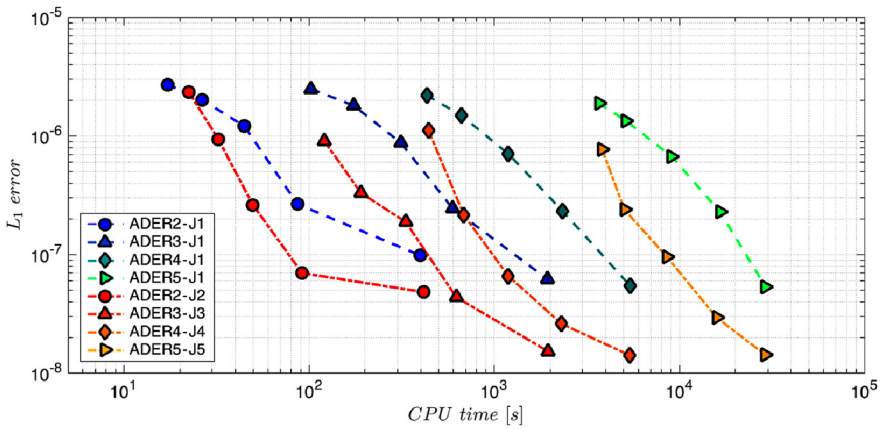

Fig. 15. Efficiency plot for a network of arteries: L_1 errors against computational times. Comparison is shown between ADER schemes of different orders, used in conjunction with the MT-HEOC solver. L_1 errors were evaluated considering the flows $q = Au$ in the whole arterial system; for a reference solution we used the fully fifth-order ADER scheme with a mesh size of 0.125 cm. Blue-shaded and red-shaded colors refer to partial and fully high orders, respectively. For interpretation of the references to color in this figure legend, the reader is referred to the web version of this article.

junction. Schemes of up to fifth order in space and time have been tested. The numerical experiments have shown that it is imperative to match the accuracy of the schemes at junctions to that in the interior of the domain. Otherwise the overall accuracy is lost. In addition, we have proposed a test problem for blood vessel networks in which there is a stiff source term. Our implicit method performed as expected, it endures the proposed test problem, while an explicit solver fails after few time steps. We have also deployed the present numerical techniques to simulate the physical model of 37 compliant silicon tubes (arteries) and 21 junctions proposed by Matthys et al. [46]. Again, in this application it is clearly seen that the accuracy of the scheme at junctions is crucial to maintain the overall accuracy. Otherwise, low-order errors travel through the network of vessels with a damping effect, for example, for the pressure pulse-waves. The proposed methodology can be applied to more general network problems if high order of accuracy is desired.

References

[1] M. Banda, M. Herty, A. Klar, Coupling conditions for gas networks governed by the isothermal Euler equations, Netw. Heterog. Media 1 (2) (2006) 295–314, http://dx.doi.org/10.3934/nhm.2006.1.295.

[2] J. Brouwer, I. Gasser, M. Herty, Gas pipeline models revisited: model hierarchies, nonisothermal models, and simulations of networks, Multiscale Model. Simul. 9 (2) (2011) 601–623, http://dx.doi.org/10.1137/100813580.

[3] P. Bales, O. Kolb, J. Lang, Hierarchical modelling and model adaptivity for gas flow on networks, in: Lecture Notes in Computer Science, Springer, 2009, pp. 337–346.

[4] G.M. Coclite, M. Garavello, B. Piccoli, Traffic flow on a road network, SIAM J. Math. Anal. 36 (6) (2005) 1862–1886, http://dx.doi.org/10.1137/s0036141004402683.

[5] R. Borsche, A. Klar, S. Kühn, A. Meurer, Coupling traffic flow networks to pedestrian motion, Math. Models Methods Appl. Sci. 24 (2) (2014) 359–380, http://dx.doi.org/10.1142/s0218202513400113.

[6] G. Bretti, R. Natalini, B. Piccoli, Numerical algorithms for simulations of a traffic model on road networks, J. Comput. Appl. Math. 210 (1–2) (2007) 71–77, http://dx.doi.org/10.1016/j.cam.2006.10.057.

[7] R. Borsche, A. Klar, Flooding in urban drainage systems: coupling hyperbolic conservation laws for sewer systems and surface flow, Int. J. Numer. Methods Fluids 76 (11) (2014) 789–810, http://dx.doi.org/10.1002/fld.3957.

[8] G. Kesserwani, R. Ghostine, J. Vazquez, R. Mosé, M. Abdallah, A. Ghenaim, Simulation of subcritical flow at open-channel junction, Adv. Water Resour. 31 (2) (2008) 287–297, http://dx.doi.org/10.1016/j.advwatres.2007.08.007.

[9] L.O. Mueller, E.F. Toro, A global multiscale mathematical model for the human circulation with emphasis on the venous system, Int. J. Numer. Methods Biomed. Eng. 30 (7) (2014) 681–725, http://dx.doi.org/10.1002/cnm.2622.

[10] L.O. Mueller, E.F. Toro, Enhanced global mathematical model for studying cerebral venous blood flow, J. Biomech. 47 (13) (2014) 3361–3372, http://dx.doi.org/10.1016/j.jbiomech.2014.08.005.

[11] J. Alastruey, A.W. Khir, K.S. Matthys, P. Segers, S.J. Sherwin, P.R. Verdonck, K.H. Parker, J. Peiró, Pulse wave propagation in a model human arterial network: assessment of 1-d visco-elastic simulations against in vitro measurements, J. Biomech. 44 (12) (2011) 2250–2258, http://dx.doi.org/10.1016/j.jbiomech.2011.05.041.

[12] L. Formaggia, F. Nobile, A. Quarteroni, A. Veneziani, Multiscale modelling of the circulatory system: a preliminary analysis, Comput. Vis. Sci. 2 (2–3) (1999) 75–83, http://dx.doi.org/10.1007/s007910050030.

[13] F. Liang, S. Takagi, R. Himeno, H. Liu, Multi-scale modeling of the human cardiovascular system with applications to aortic valvular and arterial stenoses, Med. Biol. Eng. Comput. 47 (7) (2009) 743–755, http://dx.doi.org/10.1007/s11517-009-0449-9.

[14] F. Liang, S. Takagi, R. Himeno, H. Liu, Biomechanical characterization of ventricular–arterial coupling during aging: a multi-scale model study, J. Biomech. 42 (6) (2009) 692–704, http://dx.doi.org/10.1016/j.jbiomech.2009.01.010.

[15] F. Liang, H. Senzaki, C. Kurishima, K. Sughimoto, R. Inuzuka, H. Liu, Hemodynamic performance of the Fontan circulation compared with a normal biventricular circulation: a computational model study, Am. J. Physiol., Heart Circ. Physiol. 307 (7) (2014) H1056–H1072, http://dx.doi.org/10.1152/ajpheart.00245.2014.

[16] J.P. Mynard, J.J. Smolich, One-dimensional haemodynamic modeling and wave dynamics in the entire adult circulation, Ann. Biomed. Eng. 43 (6) (2015) 1443–1460, http://dx.doi.org/10.1007/s10439-015-1313-8.

[17] M.S. Olufsen, C.S. Peskin, W.Y. Kim, E.M. Pedersen, A. Nadim, J. Larsen, Numerical simulation and experimental validation of blood flow in arteries with structured-tree outflow conditions, Ann. Biomed. Eng. 28 (11) (2000) 1281–1299, http://dx.doi.org/10.1114/1.1326031.

[18] A. Bressan, S. Čanić, M. Garavello, M. Herty, B. Piccoli, Flows on networks: recent results and perspectives, EMS Surv. Math. Sci. 1 (1) (2014) 47–111, http://dx.doi.org/10.4171/emss/2.

[19] S.W. Hong, C. Kim, A new finite volume method on junction coupling and boundary treatment for flow network system analyses, Int. J. Numer. Methods Fluids 65 (6) (2011) 707–742, http://dx.doi.org/10.1002/fld.2212.

[20] L. Formaggia, J. Gerbeau, F. Nobile, A. Quarteroni, On the coupling of 3D and 1D Navier–Stokes equations for flow problems in compliant vessels, Comput. Methods Appl. Mech. Eng. 191 (6–7) (2001) 561–582, http://dx.doi.org/10.1016/s0045-7825(01)00302-4.

[21] E. Miglio, S. Perotto, F. Saleri, Model coupling techniques for free-surface flow problems: Part I, Nonlinear Anal.: Theory Methods Appl. 63 (5–7) (2005) e1885–e1896, http://dx.doi.org/10.1016/j.na.2005.03.083.

[22] E. Miglio, S. Perotto, F. Saleri, Model coupling techniques for free-surface flow problems: Part II, Nonlinear Anal.: Theory Methods Appl. 63 (5–7) (2005) e1897–e1908, http://dx.doi.org/10.1016/j.na.2005.03.085.

[23] J.M. Fullana, S. Zaleski, A branched one-dimensional model of vessel networks, J. Fluid Mech. 621 (2009) 183, http://dx.doi.org/10.1017/s0022112008004771.

[24] R.M. Colombo, M. Garavello, On the Cauchy problem for the p-system at a junction, SIAM J. Math. Anal. 39 (5) (2008) 1456–1471, http://dx.doi.org/10.1137/060665841.

[25] R.M. Colombo, M. Herty, V. Sachers, On 2×2 conservation laws at a junction, SIAM J. Math. Anal. 40 (2) (2008) 605–622, http://dx.doi.org/10.1137/070690298.

[26] R.M. Colombo, M. Garavello, A well posed Riemann problem for the p-system at a junction, Netw. Heterog. Media 1 (3) (2006) 495–511, http://dx.doi.org/10.3934/nhm.2006.1.495.

[27] S. Sherwin, V. Franke, J. Peiró, K. Parker, One-dimensional modelling of a vascular network in space–time variables, J. Eng. Math. 47 (3/4) (2003) 217–250, http://dx.doi.org/10.1023/b:engi.0000007979.32871.e2.

[28] G.A. Reigstad, T. Flåtten, N.E. Haugen, T. Ytrehus, Coupling constants and the generalized Riemann problem for isothermal junction flow, J. Hyperbolic Differ. Equ. 12 (1) (2015) 37–59, http://dx.doi.org/10.1142/s0219891615500022.

[29] E.F. Toro, R.C. Millington, L.A.M. Nejad, Towards very high order Godunov schemes, in: Godunov Methods, Springer, 2001, pp. 907–940.

[30] T. Schwartzkopff, M. Dumbser, C.-D. Munz, Fast high order ADER schemes for linear hyperbolic equations, J. Comput. Phys. 197 (2) (2004) 532–539, http://dx.doi.org/10.1016/j.jcp.2003.12.007.
[31] T. Schwartzkopff, C.D. Munz, E.F. Toro, ADER: high-order approach for linear hyperbolic systems in 2D, J. Sci. Comput. 17 (1/4) (2002) 231–240, http://dx.doi.org/10.1023/a:1015160900410.
[32] V.A. Titarev, E.F. Toro, ADER: arbitrary high order Godunov approach, J. Sci. Comput. 17 (1/4) (2002) 609–618, http://dx.doi.org/10.1023/a:1015126814947.
[33] V. Titarev, E. Toro, ADER schemes for three-dimensional non-linear hyperbolic systems, J. Comput. Phys. 204 (2) (2005) 715–736, http://dx.doi.org/10.1016/j.jcp.2004.10.028.
[34] M. Dumbser, M. Käser, Arbitrary high order non-oscillatory finite volume schemes on unstructured meshes for linear hyperbolic systems, J. Comput. Phys. 221 (2) (2007) 693–723, http://dx.doi.org/10.1016/j.jcp.2006.06.043.
[35] M. Dumbser, M. Käser, E.F. Toro, An arbitrary high-order discontinuous Galerkin method for elastic waves on unstructured meshes – V. Local time stepping and p-adaptivity, Geophys. J. Int. 171 (2) (2007) 695–717, http://dx.doi.org/10.1111/j.1365-246x.2007.03427.x.
[36] M. Dumbser, Arbitrary-Lagrangian–Eulerian ADER-WENO finite volume schemes with time-accurate local time stepping for hyperbolic conservation laws, Comput. Methods Appl. Mech. Eng. 280 (2014) 57–83, http://dx.doi.org/10.1016/j.cma.2014.07.019.
[37] E.F. Toro, V.A. Titarev, Solution of the generalized Riemann problem for advection–reaction equations, Proc. R. Soc. A, Math. Phys. Eng. Sci. 458 (2002) (2002) 271–281, http://dx.doi.org/10.1098/rspa.2001.0926.
[38] C. Castro, E. Toro, Solvers for the high-order Riemann problem for hyperbolic balance laws, J. Comput. Phys. 227 (4) (2008) 2481–2513, http://dx.doi.org/10.1016/j.jcp.2007.11.013.
[39] A. Harten, B. Engquist, S. Osher, S.R. Chakravarthy, Uniformly high order accurate essentially non-oscillatory schemes, III, in: Upwind and High-Resolution Schemes, Springer, 1987, pp. 218–290.
[40] M. Dumbser, C. Enaux, E.F. Toro, Finite volume schemes of very high order of accuracy for stiff hyperbolic balance laws, J. Comput. Phys. 227 (8) (2008) 3971–4001, http://dx.doi.org/10.1016/j.jcp.2007.12.005.
[41] G.I. Montecinos, E.F. Toro, Reformulations for general advection–diffusion–reaction equations and locally implicit ADER schemes, J. Comput. Phys. 275 (2014) 415–442, http://dx.doi.org/10.1016/j.jcp.2014.06.018.
[42] E.F. Toro, G.I. Montecinos, Implicit, semi-analytical solution of the generalized Riemann problem for stiff hyperbolic balance laws, J. Comput. Phys. 303 (2015) 146–172, http://dx.doi.org/10.1016/j.jcp.2015.09.039.
[43] R. Borsche, J. Kall, ADER schemes and high order coupling on networks of hyperbolic conservation laws, J. Comput. Phys. 273 (2014) 658–670, http://dx.doi.org/10.1016/j.jcp.2014.05.042.
[44] L.O. Müller, P.J. Blanco, A high order approximation of hyperbolic conservation laws in networks: application to one-dimensional blood flow, J. Comput. Phys. 300 (2015) 423–437, http://dx.doi.org/10.1016/j.jcp.2015.07.056.
[45] R. Borsche, J. Kall, High order numerical methods for networks of hyperbolic conservation laws coupled with ODEs and lumped parameter models, arXiv:1507.07772, 2015.
[46] K.S. Matthys, J. Alastruey, J. Peiró, A.W. Khir, P. Segers, P.R. Verdonck, K.H. Parker, S.J. Sherwin, Pulse wave propagation in a model human arterial network: assessment of 1-d numerical simulations against in vitro measurements, J. Biomech. 40 (15) (2007) 3476–3486, http://dx.doi.org/10.1016/j.jbiomech.2007.05.027.
[47] E.F. Toro, A. Siviglia, Flow in collapsible tubes with discontinuous mechanical properties: mathematical model and exact solutions, Commun. Comput. Phys. 13 (2013) 361–385, http://dx.doi.org/10.4208/cicp.210611.240212a.
[48] L. Formaggia, A. Quarteroni, A. Veneziani, Cardiovascular Mathematics, Modeling and Simulation of the Circulatory System, Springer, 2009.
[49] P.J. Blanco, S.M. Watanabe, E.A. Dari, M.A.R.F. Passos, R.A. Feijóo, Blood flow distribution in an anatomically detailed arterial network model: criteria and algorithms, Biomech. Model. Mechanobiol. 13 (6) (2014) 1303–1330, http://dx.doi.org/10.1007/s10237-014-0574-8.
[50] D. Elad, D. Katz, E. Kimmel, S. Einav, Numerical schemes for unsteady fluid flow through collapsible tubes, J. Biomed. Eng. 13 (1) (1991) 10–18, http://dx.doi.org/10.1016/0141-5425(91)90038-9.
[51] B.S. Brook, S.A.E.G. Falle, T.J. Pedley, Numerical solutions for unsteady gravity-driven flows in collapsible tubes: evolution and roll-wave instability of a steady state, J. Fluid Mech. 396 (1999) 223–256, http://dx.doi.org/10.1017/S0022112099006084.
[52] E.F. Toro, Brain venous haemodynamics, neurological diseases and mathematical modelling. A review, Appl. Math. Comput. 272 (2016) 542–579, http://dx.doi.org/10.1016/j.amc.2015.06.066.
[53] E.F. Toro, Riemann Solvers and Numerical Methods for Fluid Dynamics, 3rd ed., Springer, 2009.
[54] G. Montecinos, C. Castro, M. Dumbser, E. Toro, Comparison of solvers for the generalized Riemann problem for hyperbolic systems with source terms, J. Comput. Phys. 231 (19) (2012) 6472–6494, http://dx.doi.org/10.1016/j.jcp.2012.06.011.
[55] C.R. Goetz, A. Iske, Approximate solutions of generalized Riemann problems for nonlinear systems of hyperbolic conservation laws, Math. Comput. 85 (297) (2015) 35–62, http://dx.doi.org/10.1090/mcom/2970.
[56] A. Harten, P.D. Lax, B. van Leer, On upstream differencing and Godunov-type schemes for hyperbolic conservation laws, SIAM Rev. 25 (1) (1983) 35–61, http://dx.doi.org/10.1137/1025002.
[57] G. Montecinos, E. Toro, Solver for the generalized Riemann problem for balance laws with stiff source terms: the scalar case, in: Theory, Numerics and Applications (in 2 volumes), World Scientific Pub. Co. Pte. Lt., 2012, pp. 576–583.
[58] A. Siviglia, M. Toffolon, Steady analysis of transcritical flows in collapsible tubes with discontinuous mechanical properties: implications for arteries and veins, J. Fluid Mech. 736 (2013) 195–215, http://dx.doi.org/10.1017/jfm.2013.542.
[59] E.F. Toro, A. Siviglia, Simplified blood flow model with discontinuous vessel properties: analysis and exact solutions, in: Modeling of Physiological Flows, Springer, 2012, pp. 19–39.
[60] E. Han, G. Warnecke, E.F. Toro, A. Siviglia, On Riemann solutions to weakly hyperbolic systems: Part 1. Modelling subcritical flows in arteries, NI15003-NPA, Isaac Newton Institute for Mathematical Sciences, University of Cambridge, UK, January 2015.
[61] E. Han, G. Warnecke, E.F. Toro, A. Siviglia, On Riemann solutions to weakly hyperbolic systems: Part 2. Modelling supercritical flows in arteries, NI15004-NPA, Isaac Newton Institute for Mathematical Sciences, University of Cambridge, UK, January 2015.
[62] S.J. Sherwin, L. Formaggia, J. Peiró, V. Franke, Computational modelling of 1D blood flow with variable mechanical properties and its application to the simulation of wave propagation in the human arterial system, Int. J. Numer. Methods Fluids 43 (6–7) (2003) 673–700, http://dx.doi.org/10.1002/fld.543.
[63] S. Tan, C.-W. Shu, Inverse Lax–Wendroff procedure for numerical boundary conditions of conservation laws, J. Comput. Phys. 229 (21) (2010) 8144–8166, http://dx.doi.org/10.1016/j.jcp.2010.07.014.
[64] L.O. Müller, G. Montecinos, E. Toro, Some issues in modelling venous haemodynamics, in: Numerical Methods for Hyperbolic Equations, Informa UK Limited, 2012, pp. 347–354.
[65] L.O. Müller, E.F. Toro, Well-balanced high-order solver for blood flow in networks of vessels with variable properties, Int. J. Numer. Methods Biomed. Eng. 29 (12) (2013) 1388–1411, http://dx.doi.org/10.1002/cnm.2580.